A metabolic function of FGFR3-TACC3 gene fusions in cancer

Véronique Frattini, Stefano M Pagnotta, Dr Tala, Jerry J Fan, Marco V Russo, Sang Bae Lee, Luciano Garofano, Jing Zhang, Peiguo Shi, Genevieve Lewis, et al.

A metabolic function of *FGFR3–TACC3* gene fusions in cancer

Véronique Frattini[1]*, Stefano M. Pagnotta[1,2]*, Tala[1], Jerry J. Fan[3,4], Marco V. Russo[1], Sang Bae Lee[1], Luciano Garofano[1,2,5], Jing Zhang[1], Peiguo Shi[1], Genevieve Lewis[1], Heloise Sanson[1], Vanessa Frederick[1], Angelica M. Castano[1], Luigi Cerulo[2,5], Delphine C. M. Rolland[6], Raghvendra Mall[7], Karima Mokhtari[8,9,10], Kojo S. J. Elenitoba-Johnson[6], Marc Sanson[8,10,11], Xi Huang[3,4], Michele Ceccarelli[2,5], Anna Lasorella[1,12,13]§ & Antonio Iavarone[1,12,14]§

Chromosomal translocations that generate in-frame oncogenic gene fusions are notable examples of the success of targeted cancer therapies[1–3]. We have previously described gene fusions of *FGFR3-TACC3* (F3–T3) in 3% of human glioblastoma cases[4]. Subsequent studies have reported similar frequencies of F3–T3 in many other cancers, indicating that F3–T3 is a commonly occuring fusion across all tumour types[5,6]. F3–T3 fusions are potent oncogenes that confer sensitivity to FGFR inhibitors, but the downstream oncogenic signalling pathways remain unknown[2,4–6]. Here we show that human tumours with F3–T3 fusions cluster within transcriptional subgroups that are characterized by the activation of mitochondrial functions. F3–T3 activates oxidative phosphorylation and mitochondrial biogenesis and induces sensitivity to inhibitors of oxidative metabolism. Phosphorylation of the phosphopeptide PIN4 is an intermediate step in the signalling pathway of the activation of mitochondrial metabolism. The F3–T3–PIN4 axis triggers the biogenesis of peroxisomes and the synthesis of new proteins. The anabolic response converges on the PGC1α coactivator through the production of intracellular reactive oxygen species, which enables mitochondrial respiration and tumour growth. These data illustrate the oncogenic circuit engaged by F3–T3 and show that F3–T3-positive tumours rely on mitochondrial respiration, highlighting this pathway as a therapeutic opportunity for the treatment of tumours with F3–T3 fusions. We also provide insights into the genetic alterations that initiate the chain of metabolic responses that drive mitochondrial metabolism in cancer.

To investigate the transcriptional changes elicited by F3–T3, we expressed F3–T3 in immortalized human astrocytes and compared gene expression profiles of cells treated with a specific inhibitor against FGFR tyrosine kinase (TK, PD173074) or vehicle. Human astrocytes expressing F3–T3 were also compared to human astrocytes that expressed kinase-dead F3–T3 (F3–T3(K508M)) or were transduced with an empty vector (Extended Data Fig. 1a). Hierarchical clustering based on genes that were differentially expressed between F3–T3 human astrocytes and PD173074-treated F3–T3 cells showed that F3–T3 human astrocytes differed from the other three groups (Fig. 1a and Extended Data Fig. 1b). Analysis of a Gene Ontology enrichment map showed that, in addition to the expected enrichment for mitotic activity[4], oxidative phosphorylation and mitochondrial biogenesis were the most significant categories to be enriched in F3–T3 human astrocytes for each of the three independent comparisons (Fig. 1b, Extended Data Fig. 1c and Supplementary Table 1). We confirmed the expression changes of mitochondrial genes by quantitative PCR with reverse transcription (RT–qPCR) (Extended Data Fig. 1d).

Compared to human astrocytes expressing the empty vector or F3–T3(K508M), F3–T3 human astrocytes exhibited increased levels of mitochondrial DNA, mitochondrial mass (MitoTracker Red) and produced higher levels of ATP (Fig. 1c, d and Extended Data Fig. 1e). F3–T3 increased respiratory complex proteins (SDHB, UQCRC1 and ATP5A1) and the mitochondrial membrane transporter VDAC1 (Extended Data Fig. 1f). We also found higher levels of VDAC1 and NDUFS4 in tumours generated from mouse glioma stem cells (mGSCs) expressing human F3–T3 and small hairpin RNA (shRNA) against *Trp53* (shTrp53) (hereafter F3–T3;shTrp53) than in tumours formed by mGSCs expressing oncogenic HRAS(12V) and shTrp53 (hereafter HRAS(12V);shTrp53)[4,7] (Extended Data Fig. 1g). Introduction of F3–T3 in human astrocytes, RPE and U251 cells increased the basal and maximal oxygen consumption rate (OCR) of these cells compared to cells transduced with F3–T3(K508M) or empty vector and this effect was reversed by FGFR-TK inhibition with AZD4547 in cells expressing exogenous F3–T3 and human glioblastoma (GBM)-derived GSC1123 cells with endogenous F3–T3[4] (Fig. 1e and Extended Data Fig. 2a–d). F3–T3 elicited only a mild increase in the extracellular acidification rate (ECAR), leading to an increase in the OCR:ECAR ratio (Extended Data Fig. 2e, f). After treatment with the inhibitor of ATP synthase oligomycin, F3–T3 human astrocytes displayed reduced ATP levels and cell growth (by more than 70%) but were resistant to the substitution of glucose with galactose in the culture medium, a condition that imposes oxidative metabolism and markedly affected cell growth of human astrocytes treated with vector (Extended Data Fig. 2g, h). A 72-h treatment with the mitochondrial inhibitors metformin, menadione or tigecycline impaired growth of GSC1123 cells but was ineffective in GSC308 F3–T3-negative gliomaspheres[4] (Fig. 1f). Similarly, mitochondrial inhibitors reduced the viability of F3–T3;shTrp53 mGSCs but did not affect HRAS(12V);shTrp53 mGSCs (Fig. 1g and Extended Data Fig. 2i–k). However, tigecycline decreased COX1 and COX2, two respiratory complex subunits translated by mitochondrial ribosomes[8], and mitochondrial inhibitors reduced ATP production, indicating that these compounds were similarly active in both cell types (Extended Data Fig. 2l, m). We also found that treatment with tigecycline (50 mg kg^{-1}) suppressed tumour growth of F3–T3;shTrp53 mGSCs glioma xenografts with a more than 50% reduction in tumour

[1]Institute for Cancer Genetics, Columbia University Medical Center, New York, New York 10032, USA. [2]Department of Science and Technology, Universita' degli Studi del Sannio, Benevento 82100, Italy. [3]The Arthur and Sonia Labatt Brain Tumour Research Centre, Program in Developmental and Stem Cell Biology, The Hospital for Sick Children, Toronto, Ontario M5G 1A4, Canada. [4]Department of Molecular Genetics, University of Toronto, Toronto, Ontario M5S 1A8, Canada. [5]BIOGEM Istituto di Ricerche Genetiche 'G. Salvatore', Campo Reale, 83031 Ariano Irpino, Italy. [6]Department of Pathology and Laboratory Medicine, Perelman School of Medicine at University of Pennsylvania, Philadelphia, Pennsylvania 19104-6100, USA. [7]Qatar Computing Research Institute (QCRI), Hamad Bin Khalifa University, Doha, Qatar. [8]Sorbonne Universités UPMC Univ Paris 06, UMR S 1127, Inserm U 1127, CNRS UMR 7225, ICM, Paris 75013, France. [9]AP-HP, Groupe Hospitalier Pitié Salpêtrière, Laboratoire de Neuropathologie R Escourolle, Paris 75013, France. [10]Onconeurotek, AP-HP, Paris 75013, France. [11]AP-HP, Hôpital de la Pitié-Salpêtrière, Service de Neurologie 2, Paris 75013, France. [12]Department of Pathology and Cell Biology, Columbia University Medical Center, New York, New York 10032, USA. [13]Department of Pediatrics, Columbia University Medical Center, New York, New York 10032, USA. [14]Department of Neurology, Columbia University Medical Center, New York, New York 10032, USA.
*These authors contributed equally to this work.
§These authors jointly supervised this work.

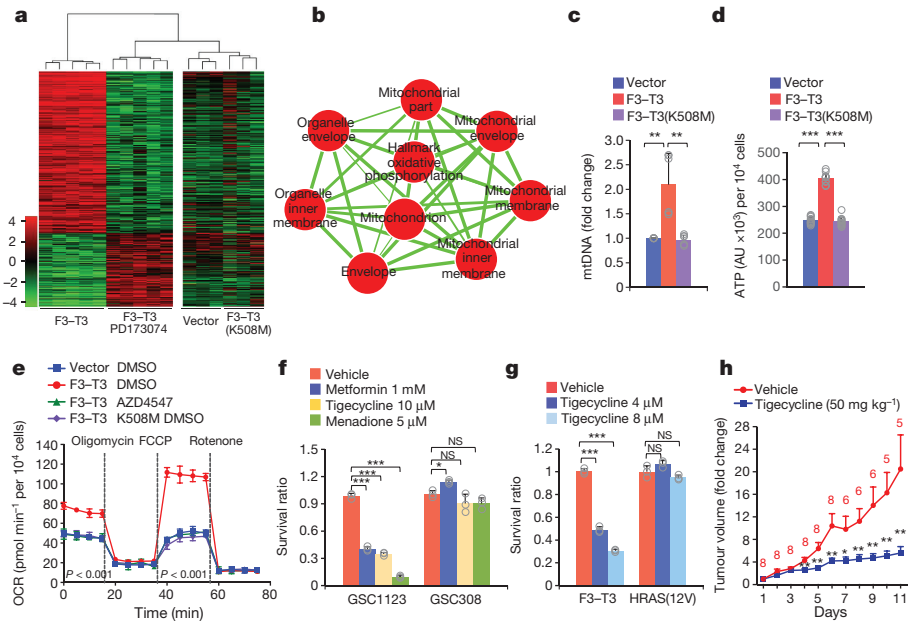

Figure 1 | Activation of mitochondrial biogenesis and metabolism by F3–T3. a, Hierarchical clustering of differentially expressed genes (DEGs) between F3–T3 human astrocytes, F3–T3 human astrocytes treated with PD173074 ($n = 5$ biologically independent samples per group). Human astrocytes expressing the empty vector and F3–T3(K508M) ($n = 3$ biologically independent samples per group) are included as controls. *t*-test $P < 0.01$ and MWW test $P < 0.01$. **b**, Enrichment map network of statistically significant GO categories ($Q < 10^{-6}$ in F3–T3 human astrocytes versus F3–T3 human astrocytes treated with PD173074 and human astrocytes expressing F3–T3(K508M) or vector). Nodes represent GO terms and lines their connectivity. Node size is proportional to the significance of enrichment and line thickness indicates the fraction of genes shared between groups. **c**, qPCR of mitochondrial DNA (mtDNA) in human astrocytes expressing F3–T3, F3–T3(K508M) or vector. **d**, Quantification of cellular ATP in human astrocytes as in **c**. **e**, OCR of F3–T3 human astrocytes treated with or without AZD4547. **f**, Survival ratio of GSC1123 and GSC308 cells following treatment with the indicated mitochondrial inhibitors. **g**, Survival ratio of F3–T3;shTrp53 and HRAS(12V);shTrp53 mGSCs treated with vehicle or tigecycline. **h**, Tumour volume in mice treated with vehicle ($n = 8$) or tigecycline ($n = 10$). Data are fold change ± s.e.m. of controls. The number of mice remaining in the study at each time point is indicated. Data are representative of two (**f**, **g**) or three (**e**) independent experiments. Data are fold change ± s.d. (**c**) or mean ± s.d. (**d**–**g**) of $n = 3$ technical replicates (**e**–**g**) or $n = 6$ (**c**) and $n = 12$ replicates (**d**) from two independent experiments. $^*P \leq 0.05$, $^{**}P \leq 0.01$, $^{***}P \leq 0.001$, two-tailed *t*-test with unequal variance.

volume after six days, the last day on which all controls were alive. At the end of the experiment (day 11), three of the eight mice in the control group had been euthanized, whereas all mice receiving tigecycline were alive ($n = 10$; Fig. 1h and Extended Data Fig. 2n).

To identify F3–T3 substrates that drive oxidative metabolism, we performed anti-phosphorylated tyrosine (phospho-tyrosine) immunoprecipitation of tryptic digests of total cellular proteins from human astrocytes expressing F3–T3, F3–T3(K508M) or the empty vector, followed by identification of phosphopeptides by liquid chromatography–tandem mass spectrometry (Supplementary Table 2). As expected, F3–T3 showed the largest changes in phospho-tyrosine; Y647 in FGFR3 and Y684 in TACC3 showed the highest and second highest enrichment in phosphorylation, respectively. After the enrichment seen in F3–T3, the next most enriched phospho-tyrosine was Y122 of PIN4 (hereafter PIN4(Y122)), a poorly studied homologue of the cancer-driver PIN1 peptidyl-prolyl-*trans*-isomerase[9–11] (Supplementary Table 2). This residue (Y122) is conserved in PIN4 across evolution and we found that F3–T3 interacts with endogenous PIN4 (Extended Data Fig. 3a, b). Analysis of anti-phosphotyrosine immunoprecipitations revealed that only cells expressing active F3–T3 contained tyrosine-phosphorylated PIN4, PKM2, DLG3, C1orf50 and GOLGIN84, whereas tyrosine-phosphorylated HGS was also present in FGFR3-expressing cells (Fig. 2a and Extended Data Fig. 3c, d). Treatment of GSC1123 cells with AZD4547 removed constitutive tyrosine phosphorylation of F3–T3, PIN4, PKM2, GOLGIN84 and C1orf50, whereas phospho-ERK, phospho-Stat3 and phospho-AKT were not changed (Extended Data Fig. 3e, f). We confirmed F3–T3-specific tyrosine phosphorylation of exogenous wild-type PIN4, PKM2, GOLGIN84, DLG3 and C1orf50, but phosphorylation of the corresponding un-phosphorylatable tyrosine to alanine or phenylalanine phospho-mutants was greatly reduced (Extended Data Fig. 3g). We generated and validated a phosphorylation-specific antibody against phosphorylated PIN4(Y122) (phospho-PIN4(Y122)). The antibody detected PIN4 in cells expressing F3–T3, but not in cells transduced with vector, FGFR3 or F3–T3(K508M) (Extended Data Fig. 3h, i). Phospho-PIN4(Y122) was readily detected in F3–T3;shTrp53 mGSCs and xenografts but was absent in HRAS(12V);shTrp53 mGSCs and corresponding tumours (Extended Data Fig. 4a, b). Immunostaining of phospho-PIN4(Y122) in primary human GBM revealed that tumours with F3–T3 ($n = 14$) expressed much higher levels of phospho-PIN4(Y122) than tumours lacking F3–T3 fusions ($n = 35$, 15 of which expressed EGFR–SEPT14, a different receptor tyrosine kinase gene fusion that signals through phospho-STAT3[12]; Fig. 2b and Extended Data Fig. 4c).

Next, we expressed wild-type and the corresponding phospho-tyrosine mutants of PIN4, PKM2, DLG3, C1orf50 and GOLGIN84 in F3–T3 human astrocytes and measured oxidative metabolism. Expression of wild-type and tyrosine to alanine or phenylalanine mutants of PKM2, DLG3, C1orf50 and GOLGIN84 failed to affect the increased OCR profile of F3–T3 human astrocytes (Extended Data Fig. 4d–g). Conversely, PIN4(Y122F) but not wild-type PIN4 (PIN4(WT)) reverted basal and maximum OCR levels of F3–T3 human astrocytes to the levels of vector-expressing human astrocytes (Fig. 2c and Extended Data Fig. 4h). We observed similar effects in F3–T3 human astrocytes in which endogenous PIN4 had been silenced and replaced by the un-phosphorylatable PIN4(Y122F) phospho-mutant (Fig. 2d and Extended Data Fig. 4i). Expression of PIN4(Y122F) and PIN4(Y122A) phospho-mutants reversed the F3–T3-mediated increase in ATP (Extended Data Fig. 4j). Expression of PIN4(Y122F) also impaired soft agar clonogenicity (Fig. 2e).

To identify the gene expression signature associated with F3–T3 in human tumours, we benchmarked different statistical methods for the analysis of imbalanced datasets using synthetic data and the

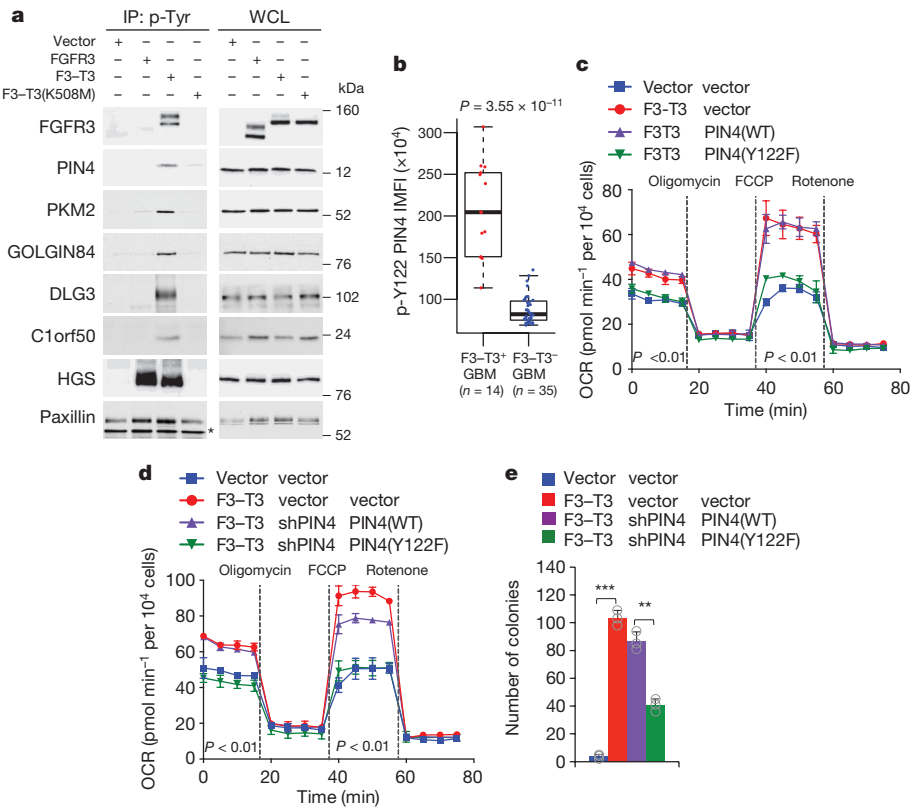

Figure 2 | Phosphorylation of PIN4 at Y122 affects mitochondrial metabolism. a, Immunoblot of phosphotyrosine immunoprecipitates from SF126 glioma cells (left) or whole-cell lysate (WCL, right). Paxillin is a loading control. IP, immunoprecipitation. **b**, Quantification of phospho-PIN4(Y122) integrated mean fluorescence intensity (IMFI) from F3–T3-positive and F3–T3-negative GBM. Box plot spans the first to third quartiles and whiskers show the 1.5× interquartile range. $P \leq 0.0001$, two-sided MWW test. **c**, OCR of F3–T3 human astrocytes transduced with PIN4(WT), PIN4(Y122F) or vector. **d**, OCR of F3–T3 human astrocytes following silencing of *PIN4* and reconstitution with PIN4(WT) or PIN4(Y122F). **e**, Soft agar colony-forming assay of human astrocytes treated as in **d**. Data in **c–e** are mean ± s.d. of one representative experiment with $n = 3$ technical replicates. Experiments were repeated three times with similar results. $^{**}P \leq 0.01$, $^{***}P \leq 0.001$, two-tailed *t*-test with unequal variance.

GBM transcriptome from The Cancer Genome Atlas (TCGA)[13]. The combination of the easy ensemble (ee) undersampling technique and Mann–Whitney–Wilcoxon (MWW) test statistics (ee-MWW) exhibited the best performance for correct identification of imbalanced samples and reproducible clustering (Supplementary Information and Supplementary Table 3). We used ee-MWW to generate a ranked list of genes discriminating F3–T3-positive samples in the GBM dataset of the TCGA and built a hierarchical cluster (confirmed by consensus clustering), including a small cluster of nine F3–T3-positive samples and nine fusion-like GBM (Fig. 3a, Extended Data Fig. 5a and Supplementary Table 4). The most significant biological processes enriched in F3–T3-positive GBM were mitochondrial categories (Fig. 3b and Extended Data Fig. 5b). Mitochondrial functions were also increased in fusion-like GBM, which were enriched for amplification and high expression of mitochondrial RNA polymerase (*POLRMT*, Extended Data Fig. 5c–e). Immunostaining of oxidative phosphorylation biomarkers in an independent GBM cohort revealed that F3–T3-positive tumours expressed higher levels of mitochondrial proteins (Fig. 3c and Extended Data Fig. 5f). The ee-MWW method clustered tumours with other rare oncogenes (oncogenic *RAS* in GBM and invasive breast carcinoma, *EGFR-SEPT14* gene fusion in GBM[12]) and identified their associated biological functions (Extended Data Fig. 5g–i and Supplementary Table 5). Using ee-MWW, we detected small and homogeneous clusters of F3–T3-positive tumours enriched for mitochondrial categories in each tumour containing recurrent F3–T3 fusions in the TCGA dataset (pan-glioma, lung squamous cell carcinoma, head and neck squamous cell carcinoma, oesophageal carcinoma, urothelial bladder carcinoma and cervical squamous cell carcinoma and endocervical adenocarcinoma; Extended Data Fig. 6a–k and Supplementary Table 6). The transcriptional similarity of F3–T3-positive glioma was confirmed by Topological Data Analysis[14,15] (Extended Data Fig. 6l). Finally, expression of the *F3–T3* fusion gene correlated with mitochondrial activities in the analysis of multiple cancer types (Extended Data Fig. 6m).

To identify the transcription factors that are causally related to the gene expression signature that is activated in F3–T3-positive glioma (master regulators)[16], we assembled transcriptional networks from the GBM and pan-glioma datasets using the regularized gradient boosting machine algorithm that was developed for the inference of gene regulatory networks[17]. In both datasets, the two most active master regulators of F3–T3-positive tumours were *PPARGC1A* and *ESRRG* (encoding the PGC1α transcriptional coactivator and the nuclear receptor ERRγ, respectively; Fig. 3d, Extended Data Fig. 6n and Supplementary Table 7). Expression of *PPARGC1A* and *ESRRG* mRNA was higher in F3–T3-positive than F3–T3-negative GBM (Extended Data Fig. 6o). Because PGC1α is a coactivator of the oestrogen-related receptor (ERR) subfamily of nuclear receptors and acts as a master regulator of mitochondrial biogenesis and metabolism[18,19], we investigated whether PGC1α and ERRγ enable the mitochondrial functions induced by F3–T3. Introduction of F3–T3 in human astrocytes expressing PIN4(WT) increased *PPARGC1A* mRNA and PGC1α protein and the expression of genes involved in reactive oxygen species (ROS) detoxification[20] (Extended Data Fig. 7a–d and Supplementary Table 7). Accordingly, PGC1α accumulated at higher levels in F3–T3-positive GSC1123 cells and F3–T3;shTrp53 mGSCs compared to F3–T3-negative GSC308 cells and HRAS(12V);shTrp53 mGSCs, respectively (Fig. 3e). However, replacement of PIN4 with the un-phosphorylatable Y122F mutant PIN4(Y122F) blunted

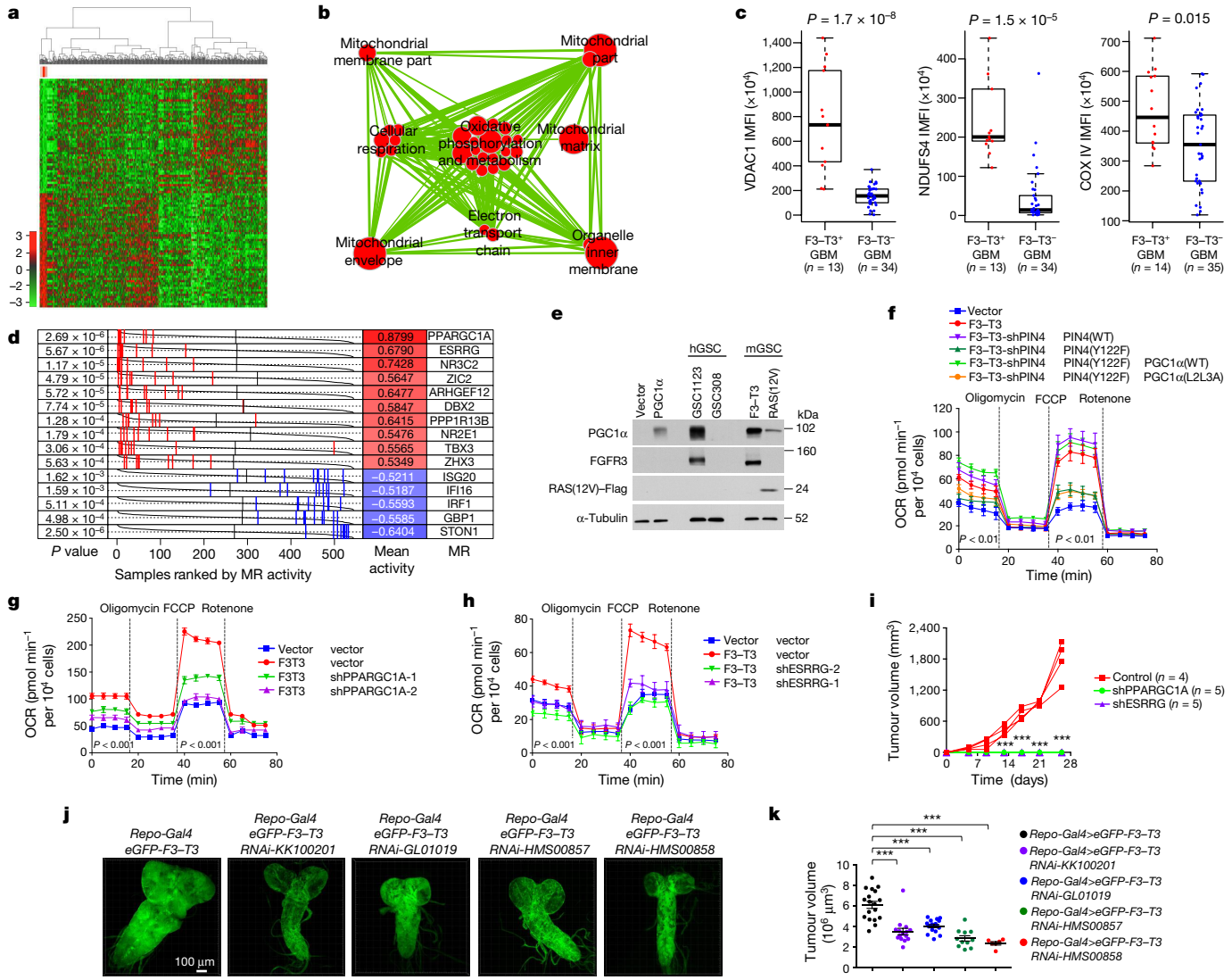

Figure 3 | PGC1α and ERRγ are required for F3–T3-mediated mitochondrial metabolism and tumorigenesis. a, Hierarchical clustering of GBM ($n = 534$) and normal brain ($n = 10$) from the TCGA using DEGs in nine F3–T3-positive samples (red) versus the F3-T3-negative samples. **b**, Enrichment map network of statistically significant GO categories in nine F3–T3-positive samples (upper-tailed MWW-GST $Q < 0.001$, normalized enrichment score (NES) > 0.6). Nodes represent GO terms and lines their connectivity. Node size is proportional to number of genes in the GO category and line thickness indicates the fraction of genes shared between groups. **c**, Quantification of IMFI of VDAC1, NDUFS4 and COXIV in F3–T3-positive and F3–T3-negative GBM. Box plot spans the first to third quartiles and whiskers show the 1.5× interquartile range. $P \leq 0.0001$ (VDAC and NDUFS4); $P \leq 0.05$ (COXIV), two-sided MWW test. **d**, Master regulator (MR) activity in GBM. Grey curves represent the activity of each master regulator. Red or blue lines indicate individual F3-T3-positive GBM displaying high or low master regulator activity, respectively ($n = 534$). *P* value, two-sided MWW test for differential activity (left) and mean of the activity (right) of the master regulator in F3–T3-positive versus F3–T3-negative samples are indicated. **e**, Immunoblot of PGC1α, in human (h) and mouse (m)GSCs. Human astrocytes transduced with PGC1α or vector are controls. **f**, OCR of F3–T3 human astrocytes following silencing of *PIN4* and reconstitution with PIN4(WT) or PIN4(Y122F), in the presence or the absence of PGC1α(WT) or PGC1α(L2L3A). **g**, OCR of F3–T3 human astrocytes transduced with *PPARGC1A* shRNA. **h**, OCR of F3–T3 human astrocytes transduced with shESRRG. **i**, Tumour growth of F3–T3 human astrocytes transduced with vector ($n = 4$), *PPARGC1A* shRNA1 ($n = 5$) or *ESRRG* shRNA1 ($n = 5$). Tumour growth curves of individual mice are shown. **j**, Representative images of whole brain–ventral nerve cord complex optical projections from *repo-Gal4>F3–T3* and *repo-Gal4>F3–T3* with *srl* RNAi *Drosophila* larvae. **k**, Quantification of tumour volume of *repo-Gal4>F3–T3* and repo-Gal4>F3–T3 with *srl* RNAi *Drosophila* larvae. **f**–**h**, Data (mean ± s.d.) are from two experiments (**f**, $n = 3$ and $n = 5$ technical replicates, respectively, per experiment) or one (**g**, **h**, $n = 4$ technical replicates) experiment. **k**, Data are mean ± s.e.m. ($n = 6$–17 larvae) of one experiment. Experiments were repeated two to three times with similar results. $^{**}P \leq 0.01$, $^{***}P \leq 0.001$, two-tailed *t*-test with unequal variance (**f**–**k**).

F3–T3-mediated induction of PGC1α (Extended Data Fig. 7a, c). The inhibition of mitochondrial metabolism and reduction in soft agar clonogenicity by PIN4(Y122F) in F3–T3 human astrocytes were both rescued by overexpression of PGC1α(WT). Conversely, PGC1α(L2L3A), which contains mutations in the nuclear receptor boxes L2 and L3 that are critical for binding ERRγ[18] could not rescue F3–T3-mediated activation of mitochondrial metabolism in F3–T3 human astrocytes expressing PIN4(Y122F) (Fig. 3f and Extended Data Fig. 7e, f). Finally, loss of PGC1α by shRNA and CRISPR–Cas9 gene editing reversed the activation of mitochondrial respiration by F3–T3 and depletion of ERRγ produced similar effects (Fig. 3g, h and Extended Data Fig. 7g–m). PGC1α silencing inhibited soft agar colony formation by F3–T3 human astrocytes and impaired self-renewal of GSC1123 cells (Extended Data Fig. 7n–p). Silencing of either *PPARGC1A* or *ESRRG* prevented tumour xenograft formation of F3–T3 human astrocytes in mice (Fig. 3i and Extended Data

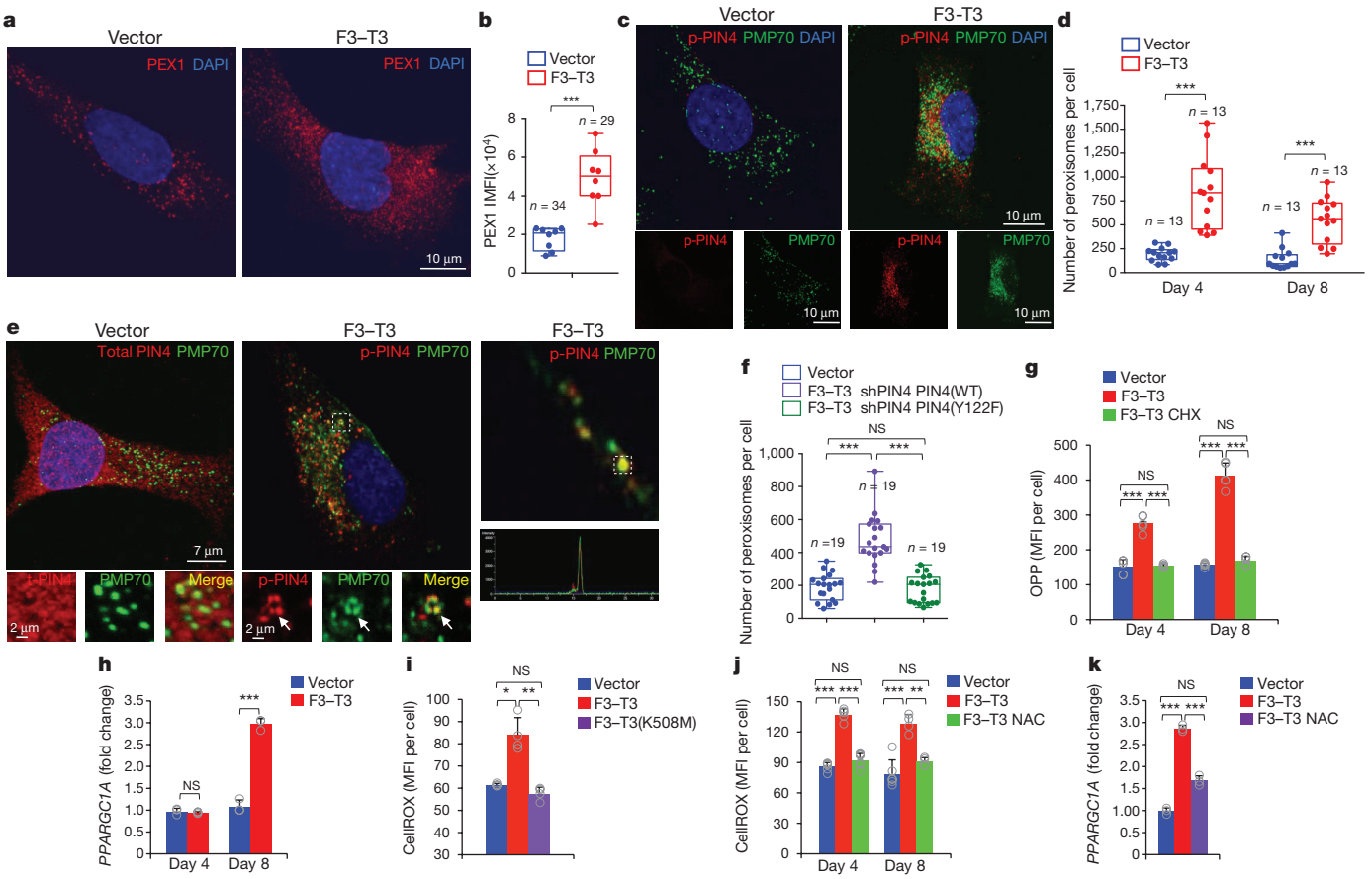

Figure 4 | Expression of F3–T3 fusion induces peroxisome biogenesis through phosphorylation of PIN4(Y122). a, Representative confocal micrographs of PEX1 immunostaining (red) and DAPI (blue) in vector and F3–T3-expressing human astrocytes. **b**, Quantification of PEX1 IMFI in samples stained as in **a** ($n = 34$ and 26 cells for vector and F3–T3, respectively). **c**, Representative confocal micrographs of double (top) and single (bottom) immunostaining for phospho-PIN4(Y122) (p-PIN4, red) and PMP70 (green) in vector and F3–T3-expressing human astrocytes. **d**, Quantification of peroxisome number per cell 4 and 8 days after F3–T3 expression in human astrocytes ($n = 13$ cells). **e**, Representative confocal micrographs of double immunostaining for total PIN4 (t-PIN4) and PMP70 in vector-expressing (left) or phospho-PIN4(Y122) and PMP70 in F3–T3-expressing (middle) human astrocytes. Arrowheads, phospho-PIN4(Y122)–PMP70 co-localization (bottom). Right, phospho-PIN4(Y122)–PMP70 co-localization (top) with corresponding spectral intensity profile (bottom); co-localization coefficients: Pearson's correlation $r = 0.935963$; Mander's overlap = 0.959905; Mander's overlap coefficients $k_1 = 0.934640$, $k_2 = 0.985853$; colocalization coefficients $c_1 = 1.000000$, $c_2 = 0.999792$. **f**, Quantification of peroxisome number per cell in F3–T3 human astrocytes following silencing of *PIN4* and expression of PIN4(WT) or PIN4(Y122F) ($n = 19$ cells). **g**, Quantification of protein biosynthesis by O-propargyl-puromycin (OPP) incorporation in human astrocytes that were treated as in **d**. Cycloheximide (CHX)-treated cultures are used as negative controls ($n = 5$ technical replicates). **h**, RT–qPCR of *PPARGC1A* in human astrocytes that were treated as in **d** ($n = 3$ technical replicates). **i**, Quantification of cellular ROS in vector-, F3–T3- and F3–T3-expressing human astrocytes. Bar graphs from one representative experiment ($n = 4$ technical replicates). **j**, Analysis of cellular ROS in human astrocytes that were treated as in **d**. Bar graphs from one representative experiment ($n = 5$ or 6 technical replicates). **k**, RT–qPCR of *PPARGC1A* in vector- or F3–T3-expressing cells that were treated with vehicle or *N*-acetyl-L-cysteine (NAC) ($n = 3$ technical replicates). Data are mean ± s.d. (**g**–**k**). *P*-values: **b**, **d**, **f**, two-sided MWW test; **g**–**k**, two-tailed *t*-test with unequal variance. Box plots span the first to third quartiles and whiskers indicate the smallest and largest values. Experiment in **i** was repeated twice; all other experiments were repeated three times with similar results.

Fig. 7q) and impaired *in vivo* tumour growth of F3–T3;shTrp53 mGSCs but not HRAS(12V)shTrp53 mGSCs (Extended Data Fig. 7r–v). Next, we developed a brain tumour model in *Drosophila* by ectopically expressing human F3–T3 using the glial-specific driver *repo-Gal4* (ref. 21). *repo-Gal4*–F3–T3 transgenic flies manifested glial neoplasia with enlargement and malformation of the larval brain lobe and ventral nerve cord, leading to larval lethality (Extended Data Fig. 8a, b). Cell number and proliferation of glial cells were enhanced in *repo-Gal4*–F3–T3 flies (Extended Data Fig. 8c, d). Cell-autonomous RNA interference (RNAi)-mediated knockdown of *spargel (srl,* the *Drosophila* orthologue of *PPARGC1A*)[22] in *repo-Gal4*–F3–T3 flies reduced glial tumour volume and decreased the number of Repo$^+$ glial cells, without affecting *repo-Gal4*-driven F3–T3 protein expression in F3–T3-expressing flies or normal brain development in wild-type animals without F3–T3 (Fig. 3j, k and Extended Data Figs 8e–g, 9a–d). *srl* knockdown did not rescue *Repo-Gal4*–F3–T3 animals to adult viability, confirming that suppressors of glial neoplasia in *Drosophila* are infrequent rescuers of organismic lethality[23] (Extended Data Fig. 9e). *srl* knockdown in a *Drosophila* model of glioma driven by constitutively active EGFR (dEGFR$^{\lambda}$) and PI3K (Dp110^{CAAX}) in the glial lineage[24] resulted in minor to no effects on tumour volume, thus highlighting the specific sensitivity of F3–T3 tumorigenesis to the perturbation of *srl* expression (Extended Data Fig. 9f, g). RNAi-mediated knockdown of the *Drosophila* oestrogen-related receptor (*ERR*) also reduced F3–T3 glial tumour volume (Extended Data Fig. 9h, i).

To determine the mechanism by which phospho-PIN4(Y122) mediates F3–T3 signalling, we studied the subcellular compartmentalization of PIN4 and phospho-PIN4(Y122) and sought to uncover the set of cellular proteins interacting with PIN4. Unphosphorylated PIN4 was diffusely localized in the cytoplasm and nuclear membrane whereas phospho-PIN4(Y122) was concentrated in larger cytoplasmic vesicle-like structures that co-localized with F3–T3 (Extended Data

Figs 3h, 10a, b). Using mass spectrometry analysis of PIN4 immunoaffinity complexes, we found that the peroxisomal biogenesis complex[25] formed by PEX1 and PEX6 is the top ranking PIN4 interactor. Other PIN4-associated proteins are implicated in vesicle formation and trafficking, nuclear and mitochondrial RNA metabolism and translation, ribosomal activity and nuclear pore/envelope functions (Extended Data Fig. 10c, d and Supplementary Table 8). Quantitative immunofluorescence revealed that PEX1 increased 2.7-fold in F3–T3 human astrocytes without changes in *PEX1* mRNA (Fig. 4a, b and Extended Data Fig. 10e, f). To investigate whether F3–T3 signals through phospho-PIN4(Y122) to promote peroxisome biogenesis, we acutely transduced human astrocytes with a F3–T3-expressing lentivirus, and found that both phospho-PIN4(Y122) and the total number of PMP70-positive peroxisomes were increased after four days (4.3 fold increase in peroxisomes per cell; Fig. 4c, d and Extended Data Fig. 10g). Phospho-PIN4(Y122)-positive cytoplasmic structures in F3–T3 human astrocytes, but not unphosphorylated PIN4 in vector-transduced human astrocytes, colocalized with PMP70, indicating that phospho-PIN4(Y122) trafficks to new peroxisomal membranes (Fig. 4e). Increased peroxisome biogenesis induced by acute expression of F3–T3 was prevented when F3–T3 was introduced in cells in which PIN4 had been replaced by the unphosphorylatable PIN4(Y122F) mutant (Fig. 4f). F3–T3 also induced a phospho-PIN4(Y122)-dependent early increase in new protein synthesis (Fig. 4g and Extended Data Fig. 10h). Conversely, PGC1α and mitochondrial gene expression were unchanged four days after acute expression of F3–T3 but increased after eight days (Fig. 4h and Extended Data Fig. 10i). Peroxisome biogenesis and new protein synthesis can both generate ROS, and ROS are crucial inducers of PGC1α[20,26,27]. F3–T3 but not F3–T3(K508M) increased ROS at the four-day time point and this effect required PIN4(Y122) phosphorylation (Fig. 4i, j and Extended Data Fig. 10j). Treatment of F3–T3 human astrocytes with the ROS inhibitor *N*-acetyl-L-cysteine eliminated approximately 70% of the increase in PGC1α induced by F3–T3 (Fig. 4k), thus indicating that ROS are responsible for most of the increase in PGC1α induced by F3–T3.

In conclusion, we describe, using an integrated computational and experimental framework, the chain of events propagated by F3–T3 in cancer. Signalling through phospho-PIN4(Y122) triggers vesicle trafficking to deliver building blocks for biogenesis of peroxisomes and new protein synthesis. The coordinated activation of these anabolic pathways results in the accumulation of ROS, which in turn increases PGC1α–ERRγ and mitochondrial metabolism. Thus, rather than impinging exclusively on mitochondrial circuits, the oncogenic signals driving mitochondrial respiration operate within larger contexts of anabolic effectors. Dependency on mitochondrial metabolism of GBM with F3–T3 suggests that inhibitors of oxidative phosphorylation may be beneficial for patients with F3–T3-positive tumours.

Online Content Methods, along with any additional Extended Data display items and Source Data, are available in the online version of the paper; references unique to these sections appear only in the online paper.

1. Ali, M. A. Chronic myeloid leukemia in the era of tyrosine kinase inhibitors: an evolving paradigm of molecularly targeted therapy. *Mol. Diagn. Ther.* **20,** 315–333 (2016).
2. Di Stefano, A. L. *et al.* Detection, characterization, and inhibition of FGFR–TACC fusions in IDH wild-type glioma. *Clin. Cancer Res.* **21,** 3307–3317 (2015).
3. Gerber, D. E. & Minna, J. D. ALK inhibition for non-small cell lung cancer: from discovery to therapy in record time. *Cancer Cell* **18,** 548–551 (2010).
4. Singh, D. *et al.* Transforming fusions of FGFR and TACC genes in human glioblastoma. *Science* **337,** 1231–1235 (2012).
5. Costa, R. *et al.* FGFR3–TACC3 fusion in solid tumors: mini review. *Oncotarget* **7,** 55924–55938 (2016).
6. Lasorella, A., Sanson, M. & Iavarone, A. FGFR–TACC gene fusions in human glioma. *Neuro-oncol.* **19,** 475–483 (2017).
7. Niola, F. *et al.* Mesenchymal high-grade glioma is maintained by the ID–RAP1 axis. *J. Clin. Invest.* **123,** 405–417 (2013).
8. Škrtić, M. *et al.* Inhibition of mitochondrial translation as a therapeutic strategy for human acute myeloid leukemia. *Cancer Cell* **20,** 674–688 (2011).
9. Uchida, T., Fujimori, F., Tradler, T., Fischer, G. & Rahfeld, J. U. Identification and characterization of a 14 kDa human protein as a novel parvulin-like peptidyl prolyl *cis/trans* isomerase. *FEBS Lett.* **446,** 278–282 (1999).
10. Uchida, T. *et al.* Pin1 and Par14 peptidyl prolyl isomerase inhibitors block cell proliferation. *Chem. Biol.* **10,** 15–24 (2003).
11. Yeh, E. S. & Means, A. R. PIN1, the cell cycle and cancer. *Nat. Rev. Cancer* **7,** 381–388 (2007).
12. Frattini, V. *et al.* The integrated landscape of driver genomic alterations in glioblastoma. *Nat. Genet.* **45,** 1141–1149 (2013).
13. He, H. & Garcia, E. A. Learning from imbalanced data. *IEEE Trans. Knowl. Data Eng.* **21,** 1263–1284 (2009).
14. Carlsson, G. Topology and data. *Bull. Am. Math. Soc.* **46,** 255–308 (2009).
15. Nicolau, M., Levine, A. J. & Carlsson, G. Topology based data analysis identifies a subgroup of breast cancers with a unique mutational profile and excellent survival. *Proc. Natl Acad. Sci. USA* **108,** 7265–7270 (2011).
16. Carro, M. S. *et al.* The transcriptional network for mesenchymal transformation of brain tumours. *Nature* **463,** 318–325 (2010).
17. Mall, R. *et al.* RGBM: regularized gradient boosting machines for the identification of transcriptional regulators of discrete glioma subtypes. Preprint at https://doi.org/10.1101/132670 (2017).
18. Devarakonda, S. *et al.* Disorder-to-order transition underlies the structural basis for the assembly of a transcriptionally active PGC-1α/ERRγ complex. *Proc. Natl Acad. Sci. USA* **108,** 18678–18683 (2011).
19. Lin, J., Handschin, C. & Spiegelman, B. M. Metabolic control through the PGC-1 family of transcription coactivators. *Cell Metab.* **1,** 361–370 (2005).
20. St-Pierre, J. *et al.* Suppression of reactive oxygen species and neurodegeneration by the PGC-1 transcriptional coactivators. *Cell* **127,** 397–408 (2006).
21. Xiong, W. C., Okano, H., Patel, N. H., Blendy, J. A. & Montell, C. repo encodes a glial-specific homeo domain protein required in the *Drosophila* nervous system. *Genes Dev.* **8,** 981–994 (1994).
22. Tiefenböck, S. K., Baltzer, C., Egli, N. A. & Frei, C. The *Drosophila* PGC-1 homologue Spargel coordinates mitochondrial activity to insulin signalling. *EMBO J.* **29,** 171–183 (2010).
23. Read, R. D. *et al.* A kinome-wide RNAi screen in *Drosophila* glia reveals that the RIO kinases mediate cell proliferation and survival through TORC2–Akt signaling in glioblastoma. *PLoS Genet.* **9,** e1003253 (2013).
24. Read, R. D., Cavenee, W. K., Furnari, F. B. & Thomas, J. B. A. A *Drosophila* model for EGFR–Ras and PI3K-dependent human glioma. *PLoS Genet.* **5,** e1000374 (2009).
25. Smith, J. J. & Aitchison, J. D. Peroxisomes take shape. *Nat. Rev. Mol. Cell Biol.* **14,** 803–817 (2013).
26. Boveris, A., Oshino, N. & Chance, B. The cellular production of hydrogen peroxide. *Biochem. J.* **128,** 617–630 (1972).
27. Han, J. *et al.* ER-stress-induced transcriptional regulation increases protein synthesis leading to cell death. *Nat. Cell Biol.* **15,** 481–490 (2013).

Supplementary Information is available in the online version of the paper.

Acknowledgements We thank C. Scuoppo for donation of the pLCiG2 plasmid and support with the gRNA design, E. Chen for identification of PIN4 immunocomplexes and H. Li for high-content microscopy. This work was supported by NIH R01CA101644, U54CA193313 and R01CA131126 to A.L.; R01CA178546, U54CA193313, R01CA179044, R01CA190891, R01NS061776 and The Chemotherapy Foundation to A.I.; SickKids Garron Family Cancer Centre Pitblado Discovery and Ontario Institute for Cancer Research (OICR) Brain Translational Research Initiative to X.H.; American Brain Tumor Association (ABTA) and a Cancer Biology Taining Grant (T32CA009503) fellowship to V.Fra.; a NRF-2013R1A6A3A03063888 fellowship to S.B.L.; an Italian Association for Cancer Research (AIRC) fellowship to M.V.R.

Author Contributions A.I. and A.L. conceived and coordinated the studies and provided overall supervision. M.C. and S.M.P. developed and performed bioinformatics analyses and wrote the computational sections. V.Fra. performed cell, molecular biology and metabolic assays, with help of T., M.V.R., A.M.C. and S.B.L. J.J.F. and X.H. developed and analysed the *Drosophila* F3–T3 model. K.S.J.E.-J. and D.M.C.R. conducted the phosphoproteomics experiments. M.S. and K.M. provided GBM tissues and assisted with immunostaining. G.L., T., V.Fre. and H.S. performed immunostaining and protein analyses. T. and P.S. performed mouse experiments. L.G., J.Z., L.C. and R.M. conducted gene expression and bioinformatics analyses. A.I. and A.L. wrote the manuscript with input from all authors.

Author Information Reprints and permissions information is available at www.nature.com/reprints. The authors declare competing financial interests: details are available in the online version of the paper. Readers are welcome to comment on the online version of the paper. Publisher's note: Springer Nature remains neutral with regard to jurisdictional claims in published maps and institutional affiliations. Correspondence and requests for materials should be addressed to A.L. (al2179@cumc.columbia.edu) or A.I. (ai2102@cumc.columbia.edu).

METHODS

Datasets. Tumour sample data are from the TCGA. Details about the cohorts and analysed samples can be found in the Supplementary Information.

Resampling methods for ranked list generation in imbalanced datasets. Preliminary testing and the ee-MWW values are reported in the Supplementary Information.

Gene Ontology networks. Gene Ontology (GO) enrichment was computed using MWW test statistics for the genes positively regulated in tumours with *FGFR3-TACC3* or other genetic alterations of interest (for example, *RAS* and *EGFR-SEPT14*). The significant GO terms from MWW-gene set test (GST) analysis (Supplementary Information) were further analysed using the Enrichment Map[28] application of Cytoscape[29]. In the network, nodes represent the terms and edges represent known term interactions and are defined by the number of shared genes between the pair of terms. Size of the nodes is proportional to statistical significance of the enrichment (Fig. 1b and Extended Data Fig. 1c) or the number of genes in the category (Fig. 3b and Extended Data Figs 5c, 6c, f, h). The overlap between gene sets is computed according to the overlap coefficient (OC), defined as:

$$\mathrm{OC} = \frac{|A \cap B|}{\min(|A|, |B|)}$$

where A and B are two gene sets, and $|X|$ equals to the number of elements within set X[30]. We set a cutoff of $\mathrm{OC} > 0.5$ to select the overlapping gene sets.

Correlation analysis between GO NES and the expression of F3–T3. We selected 19 human samples with F3–T3 fusions from ref. 31 and the TCGA fusion gene Data Portal[32]. Starting from fastq data, we applied the ChimeraScan pipeline[33] to compute the total number of reads supporting the fusion (Supplementary Table 6m). From TCGA, we obtained the legacy level 3 RNA sequencing by expectation maximization (RSEM) counts of the samples. By using the EDASeq methodology[34], we corrected the counts for GC content and applied full-quantile normalization. We transformed the normalized counts in the transcripts per million abundance quantification, applied MWW-GST to each sample and collected the NES. We used the MDSigDB collections c5.bp, c5.mf, c5.cc and hallmark collections of gene sets. We compared each gene set with the number of reads supporting the F3–T3 fusions by using the Spearman's rank correlation index (Supplementary Table 6n). To test the correlation, we assumed the alternative hypothesis of the correlation greater than zero.

Assembly of the transcriptional interactomes. To identify master regulators of the gene expression signature activated in the F3–T3-positive glioma subgroup, we first assembled independent transcriptional networks from gene expression profiles of GBM and pan-glioma datasets using the regularized gradient boosting machine algorithm (RGBM)[17] (package available from CRAN at https://cran.r-project.org/web/packages/RGBM/index.html). RGBM was used to identify regulators of the molecular subtypes of brain tumours[17,35]. We used gene expression profiles and a predefined list of 2,137 gene regulators or transcription factors (master regulators) as input. This process was independently applied to obtain GBM and pan-glioma transcriptional interactomes comprising 430,104 (median regulon size: 203) and 300,969 (median regulon size: 141) transcriptional interactions, respectively, of which 188,238 were overlapping.

Master regulator activity. To identify the master regulators of the gene expression signature activated in F3–T3-positive glioma, we modified a method that we had previously described[16]. In brief, the activity of a master regulator MR, defined as the index that quantifies the activation of the transcriptional program of that specific master regulator in each sample S_i, is calculated as follows:

$$\mathrm{Act}(S_i, \mathrm{MR}) = \frac{1}{N}\sum_{k=1}^{N} t_{ki}^{+} - \frac{1}{M}\sum_{j=1}^{M} t_{ji}^{-}$$

where t_{ki}^{+} is the expression level of the k-th positive target of the master regulator in the i-th sample, t_{ji}^{-} is the expression level of the j-th negative target of the master regulator in the i-th sample, N (or M) the number of positive (or negative) targets present in the regulon of the considered master regulator. If $\mathrm{Act}(S_i, \mathrm{MR}) > 0$, the master regulator is activated in that particular sample, if $\mathrm{Act}(S_i, \mathrm{MR}) < 0$, the master regulator is inversely activated, if $\mathrm{Act}(S_i, \mathrm{MR}) \approx 0$, it is deactivated. We used the MWW test to select master regulators that showed a significant difference between the F3–T3-positive samples and all the other samples. In Supplementary Table 7a, b, we present the list of master regulators obtained by applying master regulators analysis $\left(\left|\log_2\left(\frac{\mathrm{NES}}{1-\mathrm{NES}}\right)\right| > 2.0\right)$ and significance of differential activity <0.01.

Topological data analysis. Topological data analysis[14,15] (TDA) of the pan-glioma dataset was based on the Mapper algorithm[36]. The topological network was built using the Ayasdi platform (http://www.ayasdi.com). Several open-source implementations of Mapper are available (https://github.com/MLWave/kepler-mapper, http://danifold.net/mapper/, https://github.com/RabadanLab/sakmapper, https://github.com/paultpearson/TDAmapper). TDA was performed using the expression matrix of the top 100 genes differentially expressed between F3–T3-positive tumours and the remaining tumours as shown in Extended Data Fig. 6a. Mapper uses a dimentionality reduction algorithm and produces a topological representation of the data that preserves locality. The projection space of the dimentional-reduction algorithm is covered with overlapping bins. The data points that fall in each bin are then clustered in the original high-dimentional space. A network is constructed by assigning a node to each cluster, and clusters that share one or more samples are connected by an edge. The result is a low-dimensional network representation of the data in which nodes represent sets of samples with similar global transcriptional profiles, and edges connect nodes that have at least one sample in common. For our analysis we used 2D Locally Linear Embedding[37] as dimentional-reduction algorithm and variance normalized Euclidean metric[38] as distance. Single-linkage clustering was performed in each of the pre-images of the bins using a previously described algorithm[39]. The number of bins (resolution) for each dimension was 20 and the degree of overlap (gain) between neighbouring bins was 66%. The size of the bin was chosen such that the number of samples in each row or column of bins was the same. The open-source implementations of Mapper produce results consistent with those obtained from the Ayasdi platform[40].

Transcriptomic analysis of human astrocytes. We performed comparative analysis of gene expression of human astrocytes transduced with a lentivirus expressing F3–T3 treated with vehicle (F3–T3 and DMSO, $n = 5$ replicates), F3–T3 treated with the FGFR inhibitor PD173074 for 12 h (F3–T3 and PD173074, $n = 5$ replicates), F3–T3(K508M) treated with vehicle (F3–T3(K508M) and DMSO, $n = 3$ replicates) and empty vector treated with vehicle (vector DMSO, $n = 3$ replicates). Expression data were obtained using the Illumina human HT12v4 gene expression array. The list of 4,034 differentially expressed genes between the F3–T3 and DMSO and F3–T3 and PD173074 groups (t-test $P < 0.01$ and MWW test $P < 0.01$) was used to construct a heat map comprising the whole dataset in which vector and DMSO and F3–T3(K508M) and DMSO are control groups. Samples were clustered using the hierarchical clustering algorithm based on the Ward linkage method and Euclidean distance as implemented in R. Finally, the GO enrichment analysis was performed using the ranked list obtained from three independent comparisons: F3–T3 versus F3–T3 treated with PD173074; F3–T3 versus F3–T3(K508M); F3–T3 versus vector using the Java version of GSEA. For each comparison, statistically significant GO terms with $Q < 10^{-6}$ were selected. The statistically significant pathways common to all three comparisons were included in the construction of the visual network using the Enrichment Map application[28] of Cytoscape[29]. The microarray data have been deposited in ArrayExpress with accession number E-MTAB-6037.

Identification of proteins phosphorylated by the F3–T3 gene fusion using mass spectrometry. Cells were lysed in buffer containing 9 M urea, 20 mM HEPES pH 8.0, 0.1% SDS and a cocktail of phosphatase inhibitors. Six milligrams of protein were reduced with 4.5 mM DTT, alkylated with 10 mM iodoacetamide and digested with trypsin overnight at 37 °C. Samples were desalted on a C18 cartridge (Sep-Pak plus C18 cartridge, Waters). Each sample was prepared in triplicate. Phosphopeptide enrichments were performed as previously described[41]. An LTQ Orbitrap XL (ThermoFisher) in-line with a Paradigm MS2 HPLC (Michrom bioresources) was used to acquire high-resolution mass spectrometry and tandem mass spectrometry data. Technical duplicate data for each of the metal-oxide affinity chromatography elutions and triplicate data for the phosphotyrosine immunoprecipitation samples were acquired.

RAW files were converted to mzXML using msconvert[42] and searched against the Swissprot Human protein database (9 January 2013 release) appended with common proteomics contaminants and reverse sequences as decoys. Searches were performed with X!Tandem (version 2010.10.01.1) using the k-score plugin[43,44]. For all searches the following search parameters were used: parent monoisotopic mass error of 50 parts per million (p.p.m.); fragment ion error of 0.8 daltons; allowing for up to two missed tryptic cleavages. Variable modifications were oxidation of methionine (+15.9949@M), carbamidomethylation of cysteine (+57.0214@C), and phosphorylation of serine, threonine, and tyrosine (+79.9663@[STY]). The search results were then post-processed using PeptideProphet and ProteinProphet[45–47]. Spectral counts were obtained for each cell line using ABACUS[48]. Immunoprecipitation data of phospho-tyrosine enrichment were processed through ABACUS separately from the MOAC enrichment data. ABACUS results were filtered to only retain proteins with a ProteinProphet probability >0.7. Only phosphorylated peptides with a probability >0.8 were considered for spectral counting. For tyrosine enrichment these ABACUS parameters resulted in a protein false discovery rate (FDR) of 0.0045. This ABACUS output was used for all subsequent analysis to quantify the relative abundance of phosphorylated peptides or proteins. Phospho-site localization was performed with an in-house reimplementation of the Ascore algorithm as previously described[49]. Ascore values represent the probability of detection owing to chance, with scores

>19 corresponding to sites localized with >99% certainty. From four biological replicates, the application of stringent criteria selected 22 top-scoring candidate substrates of F3–T3 that exhibited at least a 1.5-fold enrichment in F3–T3 human astrocytes compared to human astrocytes expressing F3–T3(K508M) or the empty vector (Supplementary Table 2).

Identification of PIN4 complexes by mass spectrometry. Endogenous cellular PIN4 complexes were purified from the cell line H1299 transduced with the F3–T3-expressing lentivirus. Cellular lysates were prepared in 50 mM Tris-HCl, 250 mM NaCl, 0.2% NP40, 1 mM EDTA, 10% glycerol, protease and phosphatase inhibitors. PIN4 and mock immunoprecipitates were recovered with PIN4 antibody (Abcam, ab155283) and rabbit IgG, respectively. Immunocomplexes captured on protein A/G agarose beads were washed with lysis buffer containing 300 mM NaCl and 0.3% NP40. Bound polypeptides were eluted with the PIN4 peptide used as the epitope for the PIN4 antibody (KPVFTDPPVKTKFGYH, Abcam, ab155283). Eluates were run on SDS–PAGE gels and four gel slices were cut from the lane containing PIN4 immunoprecipitates (columns A1, B1, C1, D1; Supplementary Table 8). Four similar gel slices were cut from the lane containing control rabbit IgG immunoprecipitates (columns A2, B2, C2, D2; Supplementary Table 8). The excised gel pieces were rehydrated and digested in 80 μl of 12.5 ng μl^{-1} Trypsin Gold and 50 mM ammonium bicarbonate at 37 °C overnight. Extracted peptides were dried, reconstituted in 30 μl 0.1% TFA and stored at −20 °C before analysis.

The concentrated peptide mix was reconstituted in a solution of 2% acetonitrile (ACN), 2% formic acid (FA) and eluted from the column using a Dionex Ultimate 3000 Nano LC system. The application of a 2.0-kV distal voltage electrosprayed the eluting peptides directly into the Thermo Fusion Tribrid mass spectrometer equipped with an EASY-Spray source (Thermo Scientific). Mass spectrometer-scanning functions and HPLC gradients were controlled by the Xcalibur data system (Thermo Finnigan). Tandem mass spectra from raw files were searched against a human protein database using the Proteome Discoverer 1.4 software (Thermo Finnigan). The peptide mass search tolerance was set to 10 p.p.m. A minimum sequence length of seven amino acids residues was required. Only fully tryptic peptides were considered. Spectral counts were used for estimation of relative protein abundance between samples analysed directly on long gradient reverse phase liquid chromatography–tandem mass spectrometry. A specificity score of proteins interacting with PIN4 was computed for each polypeptide as described[50]. In brief, we compared the number of peptides identified from our mass spectrometry analysis to those reported in the CRAPome database that includes a list of potential contaminants from affinity purification–mass spectrometry experiments (http://www.crapome.org/). The specificity score is computed as $(p \times c) / S_{av} \times S_{max} \times E$, where p is the identified peptide count; c the cross-correlation score for all candidate peptides queried from the database; S_{av} the averaged spectral counts from CRAPome; S_{max} the maximal spectral counts from CRAPome; and E the total number of experiments that were found in the CRAPome database.

Cell culture. *Human cell lines.* h-TERT-immortalized human astrocytes[51], SF126 cells[52], U87 (ATCC HTB-14), h-TERT-RPE-1 (ATCC CRL-4000), HEK293T (ATCC CRL-11268), U251 (Sigma 09063001) cells. Cell lines were cultured in DMEM supplemented with 10% fetal bovine serum (FBS, Sigma). Cells were transfected using Lipofectamine 2000 (Invitrogen) or the calcium phosphate method.

Mouse glioma stem cells. F3–T3;shTrp53 and HRAS(12V);shTrp53 mGSCs were isolated from the brains of mice that had received injection of lentivirus containing a bi-cistronic expression cassette including F3–T3 or HRAS(12V) and *Trp53* shRNA into the dentate gyrus as described[4,7]. Mice showing neurological symptoms were euthanized 2–4 months after intracranial injection, and brain tumours were identified macroscopically, dissected and cultured in DMEM:F12 containing 1× N2 and B27 supplements (Invitrogen) and human recombinant FGF2 and EGF (20 ng ml^{-1} each; Peprotech). Studies were approved by the IACUC at Columbia University (AAAL7600).

Human glioma stem cells. The GBM-derived glioma stem cells (GSCs) used in this study have been described previously[4,12]. GBM-derived GSCs were grown in DMEM:F12 containing 1× N2 and B27 supplements (Invitrogen) and human recombinant FGF2 and EGF (20 ng ml^{-1} each; Peprotech). Cells were transduced using lentiviral particles in medium containing 4 μg ml^{-1} of polybrene (Sigma). Cells were routinely tested for mycoplasma contamination using the Mycoplasma Plus PCR Primer Set (Agilent Technologies) and were found to be negative. Cell authentication was performed using short-tandem repeats (STR) at the ATCC facility.

Limiting dilution assay (LDA) for human GSCs was performed as described previously[50]. In brief, spheres were dissociated into single cells and plated into 96-well plates in 0.2 ml of medium containing growth factors at increasing densities (1–100 cells per well) in triplicate. Cultures were left undisturbed for 14 days, and then the percentage of wells not containing spheres for each cell dilution was calculated and plotted against the number of cells per well. Linear regression lines were plotted, and we estimated the minimal frequency of glioma cells endowed with stem cell capacity (the number of cells required to generate at least one sphere in every well = the stem cell frequency) based on the Poisson distribution and the intersection at the 37% level using Prism 6.0 software. Data represent the means of three independent experiments performed on different days.

The soft agar colony assay was performed by seeding human astrocytes at a density of 10,000 cells per well in 6-well plates in 0.3% agar in DMEM and 10% FBS. The number of colonies per well was determined using an Olympus 1X70 microscope equipped with a digital camera.

Subcutaneous xenograft glioma models. Mice were housed in a pathogen-free animal facility. All animal studies were approved by the IACUC at Columbia University (AAAQ2459; AAAL7600). Mice were 4–6 week old male and female athymic nude (*Nu/Nu*, Charles River Laboratories). No statistical method was used to pre-determine sample size. No method of randomization was used to allocate animals to experimental groups. Mice in the same cage were generally part of the same treatment. The investigators were not blinded during outcome assessment. In none of the experiments did tumours exceed the maximum volume allowed according to our IACUC protocol, specifically, 20 mm in the maximum diameter. 5×10^5 F3–T3 human astrocytes transduced with a lentivirus expressing the shRNA sequence against *PPARGC1A* or *ESRRG* or the empty vector were injected subcutaneously in the right flank in 150 μl of saline solution (five mice per group). 0.5×10^5 F3–T3;shTrp53 mGSCs and HRAS(12V);shTrp53 mGSCs transduced with lentivirus expressing two independent shRNA sequences against *PPARGC1A* were injected subcutaneously in the right flank in 100 μl of saline solution (five mice per group). Treatment with tigecycline (10 mice) or vehicle (8 mice) was performed in mice injected with 1×10^5 F3–T3;shTrp53 mGSCs when tumours reached 150–270 mm^3 (10 days after injection). Tigecycline was diluted in saline pH 7 and administered at dose of 50 mg kg^{-1} body weight by intraperitoneal injection b.i.d. Tumour diameters were measured daily with a caliper and tumour volumes estimated using the formula: $(\text{width}^2 \times \text{length}) / 2 = V\,(\text{mm}^3)$. Mice were euthanized when tumour size reached the maximum diameter allowed by our IACUC protocol (20 mm in the maximum diameter) or when mice displayed body weight loss equal to or greater than 20% of total body mass, or showed signs of compromised health or distress.

Plasmids, cloning, and lentivirus production. cDNAs for *FGFR3*, *PIN4*, *PKM2*, *GOLGIN84*, *DLG3*, *C1ORF50* and *PPARGC1A* were amplified by PCR and cloned into the pLOC vector in frame with Flag or V5 tag. *F3–T3*, *F3–T3*^{K508M} and FLAG-tagged *PEX1* were cloned into a pLVX-puro vector (Clontech). To generate PIN4(Y122A), PIN4(Y122F), PKM2(Y105A), GOLGIN84(Y42A), DLG3(Y673A) and C1orf50(Y131A), site-directed mutagenesis was performed using the QuickChange Site-Directed mutagenesis kit (Agilent) and the resulting plasmids were sequence verified. Lentivirus was produced by co-transfection of the lentiviral vectors with pCMV-ΔR8.1 and pCMV-MD2.G plasmids into HEK293T cells as previously described[7,16]. shRNA sequences are: *PIN4* shRNA: GTCAGACACATTCTATGTGAACTCGAGTTCACATAGAATGTGTCTGAC; *PPARGC1A* Hs-shRNA1: GCAGAGTATGACGATGGTATTCTCGAGAA TACCATCGTCATACTCTGC; *PPARGC1A* Hs-shRNA2: CCGTT ATACCTGTGATGCTTTCTCGAGAAAGCATCACAGGTATAACGG; *Ppargc1a* Mm-shRNA1: CCAGAACAAGAACAACGGTTTCTCGAGAAACCGT TGTTCTTGTTCTGG; *Ppargc1a* Mm-shRNA2: CCCATTTGAGAACAAGAC TATCTCGAGATAGTCTTGTTCTCAAATGGG; *ESRRG* shRNA1: CAAACAA AGATCGACACATTGCTCGAGCAATGTGTCGATCTTTGTTTG; *ESRRG* shRNA2: CATGAAGCGCTGCAGGATTATCTCGAGATAATCCTGC AGCGCTTCATG.

For the generation of *PPARGC1A*-knockout F3–T3 human astrocytes with CRISPR–Cas9, guide RNA (gRNA) sequences were designed to target the coding sequence of *PPARGC1A* as described (http://crispr.mit.edu/). We designed two gRNAs against exon 1 of the *PPARGC1A* gene and validated three clones for loss of PGC1α expression. sgRNA sequence 1 (GGCGTGGGACATGTGCAACC) and 2 (ACCAGGACTCTGAGTCTGTA) were inserted by linker cloning in the lentiviral vector pLCiG2[53,54]. Human astrocytes expressing the empty vector or F3–T3 were infected either with pLCiG2 and control, pLCiG2 and *PPARGC1A* gRNA1 or pLCiG2 and *PPARGC1A* gRNA2. After 72 h of infection, cells were seeded in a 96-well plate at a density of 0.6 cell per well. Two weeks later, colonies were isolated and *PPARGC1A* deletion was analysed by RT–qPCR and western blot. For acute expression of F3–T3 in human astrocytes, cells were first transduced with pLOC expressing Flag–PIN4(WT) or the Y122F mutant. Subsequently, cells were transduced with a pLKO.1-puro vector encoding shRNA targeting *PIN4*. The levels of endogenous and ectopically expressed proteins were then verified by immunoblotting. Finally, cells were transduced with a pLVX vector expressing F3–T3.

Generation of phospho-PIN4(Y122) antibody. The anti-phospho-PIN4 antibody was generated by immunizing rabbits with a short synthetic peptide

containing phosphorylated Y122 (underlined) (PVKTKFGYHIIMVE) (Yenzym Antibodies, LLC). A two-step purification process was applied. First, antiserum was cross-absorbed against the phospho-peptide matrix to purify antibodies that recognized the phosphorylated peptide. Next, the anti-serum was purified against the un-phosphorylated peptide matrix to remove non-specific antibodies. Antibodies were validated using lysates from cells transfected with PIN4(WT) or the phospho-mutant PIN4(Y122A).

Immunoblot and immunoprecipitation. For western blot, cells were lysed in RIPA buffer (50 mM Tris-HCl pH 7.5, 150 mM NaCl, 1 mM EDTA, 1% NP40, 0.5% sodium dexoycholate, 0.1% sodium dodecyl sulphate, 1.5 mM Na_3VO_4, 10 mM sodium fluoride, 10 mM sodium pyrophosphate, 10 mM β-glycerolphosphate and EDTA-free protease inhibitor cocktail, Roche). Lysates were cleared by centrifugation at 15,000 r.p.m. for 15 min at 4 °C. Phospho-tyrosine immunoprecipitation was performed on cells that were freshly collected in cold PBS containing Na_3VO_4 and lysed in RIPA buffer. Subsequently, 800 μg of protein extract was incubated with 30 μl of phospho-tyrosine sepharose beads (P-Tyr-100, Cell Signaling Technology, 9419) in a final volume of 800 μl overnight at 4 °C. Beads were washed five times with cold RIPA buffer and eluted by 2× SDS sample buffer. Immunoprecipitates were separated by SDS–PAGE and transferred to a nitrocellulose membrane. Membranes were blocked in TBS with 5% non-fat milk and 0.1% Tween-20, and probed with primary antibodies overnight at 4 °C. PIN4 and Flag–PEX1 immunoprecipitation was performed on cells that were freshly collected in cold PBS and lysed in 50 mM Tris pH 8.0, 150 mM NACl, 0.5% NP40, 1 mM EDTA, 10% glycerol, protease and phosphatase inhibitors. Subsequently, 2,000 μg of protein extract was incubated with PIN4 antibody (Abcam, ab155283) at a concentration of 0.6 μg mg^{-1} cell lysate or Flag–M2 agarose beads in a final volume of 1,000 μl overnight at 4 °C. For PIN4 immunoprecipitation, Protein A/G Plus agarose beads (Santa Cruz Biotechnology) were added for 2 h at 4 °C. Beads were washed five times with cold lysis buffer including 300 mM NaCl, and immunocomplexes were eluted with PIN4 or Flag–M2 peptide at room temperature for 4 h or 45 min, respectively. Immunoprecipitates were separated by SDS–PAGE and transferred to a nitrocellulose membrane. Membranes were blocked in TBS with 5% non-fat milk and 0.1% Tween-20, and probed with primary antibodies overnight at 4 °C.

Antibodies and concentrations were: FGFR3 1:1,000 (Santa Cruz, B-9, sc-13121), PIN4 1:1,000 (Abcam, ab155283), PKM2 1:1,000 (Cell Signaling, 3198), DLG3 (also known as SAP102) 1:1,000 (Cell Signaling, 3733), GOLGIN84 1:2,000 (Santa Cruz, H-283, sc-134704), C1orf50 1:1,000 (Novus Biologicals, NBP1-81053), HGS 1:1,000 (Abcam, ab72053), FAK 1:1,000 (Cell Signaling, 3285), Paxillin 1:1,000 (BD Transduction, 610051), PGC1α 1:500 (Santa Cruz, H300, sc-13067), PGC1α 1:1,000 (Novus Biological, NBP104676), ERRγ 1:500 (Abcam, ab128930), ERRγ 1:500 (R7D, PP-H6812000), phospho-FRS2 1:1,000 (Cell Signaling, 3861), FRS2 1:1,000 (Santa Cruz, sc-8318), phospho-STAT3 1:1,000 (Cell Signaling, 9131), STAT3 1:1,000 (Santa Cruz, C-20, sc-482,), phospho-AKT 1:1,000 (Cell Signaling, 4060), AKT 1:1,000 (Cell Signaling, 9272), phospho-ERK1/2 1:1,000 (Cell Signaling, 4370), ERK1/2 1:1,000 (Cell Signaling, 9102), β-actin 1:2,000 (Sigma, A5441), PEX1 1:500 (BD Biosciences, 611719), PEX6 1:500 (Stress Marq, SMC-470), NUP214 1:500 (Abcam, ab70497), SEC16A 1:500 (Abcam, ab70722), DHX30 1:500 (Novus Biologicals, NBP1-26203), SUN-2 1:500 (Abcam, ab124916), Flag 1:1,000 (Abcam, ab1162), retinoblastoma 1:1,000 (BD Pharmingen, 554136), α-tubulin 1:2,000 (Sigma, T5168), total OXPHOS 1:1,000 (Abcam, ab110411), MTCO1 1:1,000 (Abcam, ab14705). Secondary horseradish-peroxidase-conjugated antibodies were purchased from Pierce and Enhanced ChemiLuminescence (Amersham) or Super Signal West Femto (Thermo Scientific) was used for detection.

RT–qPCR. Total RNA was prepared using the Trizol reagent (Invitrogen) and cDNA was synthesized using SuperScript II Reverse Transcriptase (Invitrogen) as described[16,55]. RT–qPCR was performed with a Roche 480 thermal cycler, using SYBR Green PCR Master Mix (Applied Biosystems). RT–qPCR results were analysed by the $\Delta\Delta C_t$ method[56] using *18S* or *Actb* as the housekeeping gene.

Human primers used for RT–qPCR were as follows. UQCRC1 forward 5′-CACC GTGATGATGCTCTACC-3′ and reverse 5′-CCACCACCATAAGTGCAGTC-3′; *POLRMT* forward 5′-TATTCATGGTGAAGGATGCC-3′ and reverse 5′-TCTGT TCCAGACACCTTTCG-3′; *NDUFB4* forward 5′-TGCTTCAGTACAACGA TCCC-3′ and reverse 5′-CACACAGAGCTCCCATGAGT-3′; *MRPL15* forward 5′-TGCTTCCACCAGAAGAACTG-3′ and reverse 5′-ACTTCCTGGCGA GTTCAAGT-3′; *MCL1* forward 5′-GCATCGAACCATTAGCAGAA-3′ and reverse 5′-TGCCACCTTCTAGGTCCTCT-3′; *MRPS30* forward 5′-TATTC CTCGTGGTCATCGAA-3′ and reverse 5′-CTCTGCGAGTTGCTTGGATA-3′; *TIMM10* forward 5′-CCTGGACCGATGTGTCTCTA-3′ and reverse 5′-GCACCCT CTTCATCAGCTCT-3′; *NRF1* forward 5′-GGAAACGGCCTCATGTATTT-3′ and reverse 5′-TCATCTAACGTGGCTCGAAG-3′; *ATP5G3* forward 5′-CCCAGAATG GTGTGTCTCAG-3′ and reverse 5′-TTCCAATACCAGCACCAGAA-3′; *ABCE1* forward 5′-TCATTGATCAAGAGGTGCAGA-3′ and reverse 5′-TAGACATC AGCAGGTTTGCC-3′; *TIMM23* forward 5′-GGATTGAAGGAAACCCAGAA-3′ and reverse 5′-CCCTTGCCTAGTCACCATATT-3′; *TFAM* forward 5′-GCTC AGAACCCAGATGCAA-3′ and reverse 5′-CACTCCGCCCTATAAGCATC-3′; *TIMM9* forward 5′-TGAAGAGACCACCTGTTCAGA-3′ and reverse 5′-AAGGAGTCCTGCTTTGGCT-3′; *TIMM44* forward 5′-TCCAA GACAGAGATGTCGGA-3′ and reverse 5′-GATGTCGTTCTCGCACTGTT-3′; *VDAC1* forward 5′-AATGTGAATGACGGGACAGA-3′ and reverse 5′-ACAGCGG TCTCCAACTTCTT-3′; *NDUFA9* forward 5′-TATGCATCGGTTTGGTCCTA-3′ and reverse 5′-GACCAACGAAAGCAAAGGAT-3′; *NDUFV2* forward 5′-AAAG GCAGAATGGGTGGTT-3′ and reverse 5′-CTTTCCAACTGGCTTTCGAT-3′; *COX5A* forward 5′-GATGCTCGCTGGGTAACATA-3′ and reverse 5′-GGGCTCTG GAACCATATCAT-3′; *NDUFS5* forward 5′-TGGTGAACAGCCCTACAAGA-3′ and reverse 5′-TCTGCCCGAGTATAACCGAT-3′; *NDUFA2* forward 5′-CGTCAG GGACTTCATTGAGA-3′ and reverse 5′-AAGGGACATTCGTCTCTTGG-3′; *PITRM1* forward 5′-TCTCGGATGAGATGAAGCAG-3′ and reverse 5′-CCCAG TGCCGAGGTATCTAT-3′; *CISD1* forward 5′-TGACTTCCAGTTCCAGCGTA-3′ and reverse 5′-GATAACCAATTGCAGCTGTCC-3′; *ATP5G1* forward 5′-AGCTCT GATCCGCTGTTGTA-3′ and reverse 5′-GGAAGTTGCTGTAGGAAGGC-3′; *MRPL12* forward 5′-TCAACGAGCTCCTGAAGAAA-3′ and reverse 5′-GTGTC CGTTCTTTCGCTATG-3′; *IDH3A* forward 5′-CCGACCATGTGTCTCTATCG-3′ and reverse 5′-GCACGACTCCATCAACAATC-3′; *18S* forward 5′-CGCCG CTAGAGGTGAAATTC-3′ and reverse 5′-CTTTCGCTCTGGTCCGTCTT-3′; *PPARGC1A* forward 5′-CTCACACCAAACCCACAGAG-3′ and reverse 5′-GTGT TGTGACTGCGACTGTG-3′; *PEX1* forward 5′-AGTCACCAGCCTGCA TTCTT-3′ and reverse 5′-ATGGGAACATGGCTTGAGAA-3′.

Mouse primers used in RT–qPCR were as follows. Ppargc1a forward 5′-GACAG CTTTCTGGGTGGATT-3′ and reverse 5′-CGCAGGCTCATTGTTGTACT-3′; *Actb* forward 5′-GATGACGATATCGCTGCGCTG-3′ and reverse 5′-GTACGACCAGAGGCATACAGG-3′.

Quantification of mitochondrial DNA content. Total DNA was isolated using the Puregene Blood Core kit (Qiagen) according to the manufacturer's instructions. Mitochondrial DNA content was measured using real-time quantitative PCR (qPCR) as previously described[57]. In brief, relative quantification of mitochondrial DNA content for each sample was determined using a set of mitochondrial specific primers: mt-Mito: forward 5′-CACTTTCCACACAGACATCA-3′, reverse 5′-TGGTTAGGCTGGTGTTAGGG-3′; and a set of nuclear-specific primers: *B2M* forward 5′-TGTTCCTGCTGGGTAGCTCT-3′ and reverse 5′-CCTCCATGATG CTGCTTACA-3′. qPCR was performed with a Roche 480 thermal cycler, using SYBR Green PCR Master Mix (Applied Biosystems). qPCR conditions used were: 95 °C for 10 min followed by 40 cycles at 95 °C for 15 s, 72 °C for 15 s followed by a melting cycle going up to 95 °C. Primer specificity was determined by melt curve analysis and agarose gel electrophoresis, confirming a single band of the amplification product. The relative mitochondrial DNA content was calculated using the $2^{-\Delta\Delta C_t}$ method where ΔC_t is $C_t^{\text{mt-Mito}} - C_t^{B2M}$.

Mitochondria analysis by flow cytometry. Cells were seeded in 60-mm dishes and cultured in DMEM containing 10% FBS. Cells were washed once with FBS-free medium. Mitotracker Red (LifeTechnologies, M7212) was added to a final concentration of 20–40 nM and incubated for 20–30 min at 37 °C. Cells were then quickly washed with PBS, trypsinized, collected in phenol-red-free medium and incubated for 10 min at 37 °C in the dark before analysis. Unstained cells were used as a negative control. Acquisition was performed on LSR II Flow Cytometer (BD Biosciences) on the basis of forward and sideward scatter parameters and Texas red fluorescence using BD FACSDiva software. Eight to ten thousand events from each sample were evaluated. Data were analysed using the FCS Express 6 Flow software (*De novo* Software).

Metabolic assays. *Measurement of oxygen consumption rate and extracellular acidification rate.* The functional status of mitochondria in cells expressing F3–T3 was determined by analysing multiple parameters of oxidative metabolism using the XF96 Extracellular Flux Analyzer (Agilent), which measures the extracellular flux changes of oxygen and protons. Cells were plated in XF96-well microplates (6,000–7,000 cells per well) in a final volume of 80 μl of DMEM medium (25 mM glucose, 2 mM glutamine) supplemented with 10% FBS, 48 h before the assay. For experiments requiring AZD4547 treatment, cells were plated as previously described in the presence of 150 nM of AZD4547. For the mitochondrial stress test, cells were washed twice with 200 μl of XF Assay Medium Modified DMEM (Agilent), supplemented with 25 mM glucose, 2 mM glutamine (XF-Mito-MEM) and incubated at 37 °C in the absence of CO_2 for 1 h before the assay in 180 μl per well of XF-Mito-MEM. The ports of the sensor cartridge were sequentially loaded with 20 μl per well of the appropriate compound: the ATP coupler oligomycin (Sigma, O4876), the uncoupling agent carbonyl cyanide 4-(trifluoromethoxy) phenylhydrazone (FCCP, Sigma C2920) and the complex I inhibitor rotenone (Sigma, R8875). Compound concentration used for the different cell lines are indicated in Supplementary Table 9a. For the glycolysis stress test, cells were washed twice with

200 µl of XF Assay Medium Modified DMEM supplemented with 2 mM glutamine (XF-Glyco-MEM) and incubated at 37 °C in the absence of CO_2 for 1 h before the assay in 180 µl per well of XF-Mito-MEM. The ports of the sensor cartridge were sequentially loaded with 20 µl per well of the appropriate compound: glucose (10 mM final concentration; Sigma, 8769), oligomycin (2 µM final concentration; Sigma, O4876) and 2-DG (100 mM final concentration; Sigma, 8375). OCR and ECAR were measured through 16 rates: 4 rates under basal conditions, 4 rates after oligomycin or glucose injection, 4 rates after FCCP or oligomycin injection, and 4 rates after rotenone or 2-DG injection, for OCR or ECAR evaluation, respectively. The protocol was: mix (2 min), wait (1 min) and measure (2 min). OCR and ECAR values were normalized to the number of cells per well. The ratio OCR:ECAR was determined by dividing the normalized value of rate 4 of the OCR (basal condition) with the normalized value of rate 8 of the ECAR (after glucose injection).

ATP assay. Cells were cultured in DMEM medium containing 25 mM glucose, 2 mM glutamine and 10% FBS. After 24 h, 5,000 cells per 130 µl were plated in opaque white 96-well plates in 5 mM glucose, 2 mM glutamine and 0.2% FBS DMEM medium. CellTiterGlo assay reagent (Promega, G7570) was added 12–16 h later, according to the manufacturer's instructions and luminescence was measured using a GloMax-Multi+ Microplate Multimode Reader (Promega). For experiments testing the effect of oligomycin, cells were cultured in glucose-free DMEM medium for 24 h and ATP levels were determined as described above.

Cell growth assay. Time-course analysis of cellular growth of human astrocytes expressing F3–T3 or the empty vector was performed by plating 12,500 cells per well in triplicate in 6-well plate in DMEM containing 10% FBS. After 24 h, cells were washed and cultured in glucose-free DMEM medium containing 0.2% FBS and supplemented with 25 mM glucose or 25 mM galactose in the presence or absence of 100 nM oligomycin. Viable cells were scored every two days by Trypan blue exclusion. Survival assays of human and mouse GSCs treated with mitochondrial inhibitors were performed by plating 25,000 cells per well in 12-well plates in triplicate. Cells were counted after 72 h.

Gene set enrichment analysis (GSEA) for ROS detoxification genes. We generated a gene set of 46 genes participating in ROS detoxification programs by combining genes extracted from specific references[20,58] and the detoxification of reactive oxygen species reactome pathway R-HSA-3299685 (http://reactome.org/pages/download-data/). The full list of genes is reported in Supplementary Table 7c. The GSEA analysis was performed comparing the gene expression of F3–T3-expressing and vector control-transduced human astrocytes using default settings[59].

Analysis of protein biosynthesis and ROS by high content microscopy. Human astrocytes transduced as indicated in the figure legends were plated at a density of 6,000 cells per well in 96-well clear-bottom black plates (Greiner) 18 h before the analysis in preparation for the evaluation of both protein biosynthesis and cellular ROS. Protein biosynthesis was detected by the Click-iT Plus OPP Alexa Fluor-594 protein synthesis assay kit (Molecular Probes, C10457). Cells were incubated in the dark with O-propargyl-puromycin (OPP) reagent at a concentration of 10 µM for 30 min. Identical samples were treated with CHX at a concentration of 30 µM for 30 min before addition of OPP reagent and used as negative controls. Samples were washed with Click-iT rinse buffer, fixed in 3.7% formaldehyde for 15 min followed by permeabilization in 0.5% Triton X-100 for 15 min. Click-iT OPP reaction cocktail was then added for 30 min followed by one wash in Click-iT rinse buffer and nuclear counterstaining with DAPI. Acquisition of fluorescence intensity was performed using an IN Cell Analyzer 2000 (GE Healthcare) equipped with a 2,048 × 2,048 CCD camera. Assay conditions were: two-colour assay (DAPI and Cy3), 20× objective, exposure time 0.5 ms for Cy3 and 0.1 ms for DAPI. Four fields around the centre of each well, including 2,000 to 6,000 cells, were imaged. Data were analysed using IN Cell Investigator software (GE Healthcare). Fluorescence intensity was normalized to the number of cells as determined by the number of DAPI-positive objects in each well.

For determination of cellular ROS, cells were incubated in the dark with CellROX Deep Red reagent at concentration of 2.5 µM for 30 min at 37 °C. Identical samples were treated with *N*-acetyl-L-cysteine at concentration of 5 µM for 2 h before addition of CellROX Deep Red reagent and used as negative controls. Samples were washed once with PBS, fixed in 3.7% formaldehyde for 15 min followed by two additional washes in PBS and nuclear counterstaining with DAPI. Acquisition of fluorescence intensity was performed as described above. Assay conditions were: two-colour assay (DAPI and Cy5), 20× objective, exposure time 0.8 ms for Cy5 and 0.1 ms for DAPI. Four fields around the centre of each well, including 2,000 to 6,000 cells, were imaged. Data were analysed using IN Cell Investigator software (GE Healthcare). Fluorescence intensity was normalized to the number of cells as determined by the number of DAPI-positive objects in each well.

Immunofluorescence of cultured cells and primary tissue. Cells were fixed with 4% paraformaldehyde containing 4% sucrose, permeabilized with 0.1–1% Triton X-100, 0.1% BSA in TBS for 4 min at 4 °C, and blocked with 3% BSA, 0.05% Triton X-100 in TBS. The primary antibodies used were as follows: phospho-PIN4 (1:100); PMP70 (Sigma, SAB4200181, 1:150); PEX1 (BD Bioscience, 611719, 1:100); FGFR3 (Santa Cruz, sc-13121 B9, 1:1,000). Secondary antibodies were anti-mouse Alexa Fluor-647, anti-rabbit Alexa Fluor-568, or Cy3-conjugated (Molecular Probes, Invitrogen). Nuclei were stained with DAPI (Sigma).

Fluorescence microscopy was performed on a Nikon A1R MP microscope using a 100×, 1.45 Plan Apo Lambda lens. Images were recorded with a *z*-optical spacing of 0.15 µm and analysed using the NIS Elements Advanced Research software (Nikon Instruments). The number of peroxisomes per cell was scored as the average of $PMP70^+$ in five *z* sections (one at the equatorial plane and two above and two below the equatorial plane). Quantification of PEX1 fluorescence intensity was performed on maximum intensity images of *z* sections. After calibration and thresholding, the integrated density (product of the area and the mean intensity value (IMFI)) was averaged between 30 cells in at least six representative pictures per sample.

Tissue preparation and immunostaining on mouse and human tissues were performed as previously described[7,50,60]. The human GBM samples analysed by immunostaining had been stored in the Onconeurotek Tumourbank (certified NF S96 900), and received the authorization for analysis from ethical comittee (CPP Ile de France VI, A39II), and French Ministry for research (AC 2013-1962). In brief, tumour sections were deparaffinized in xylene and rehydrated in a graded series of ethyl alcohol. Antigen retrieval was performed in citrate solution pH 6.0 using a decloaking chamber (10 min for phosho-PIN4 and 7 min for COXIV, VDAC, NDUFS4 and FGFR3). Primary antibodies were incubated at 4 °C overnight: COXIV (Cell Signaling, 4850, 1:1,500), VDAC1 (Abcam, ab14734, 1:700), NDUFS4 (Abcam, ab55540, 1:700), phosho-PIN4(Y122) (1:200) and FGFR3 (Santa Cruz, B9, sc-13121, 1:500). Sections were incubated in biotinylated secondary antibody for 1 h, followed by 30 min of streptavidin–HRP-conjugated (Vector Laboratories) for phosho-PIN4(Y122), FGFR3, VDAC1, and NDUFS4 or HRP-conjugated anti-rabbit secondary antibody (DAKO) for COXIV and TSA–Cy3 or TSA–Fluorescein (Perkin-Elmer). Nuclei were counterstained with DAPI (Sigma). Images were acquired using 20× magnification using an Olympus 1X70 microscope equipped with digital camera. Quantification of fluorescence intensity was performed using NIH ImageJ software. After calibrating and standardizing the 8-bit grayscale images, the integrated density (IMFI) was averaged between three 20× representative pictures per sample section.

***Drosophila* studies.** The *UAS-F3–T3* flies were generated by inserting the human F3–T3 fusion gene into the pACU2 plasmid followed by embryo injection of the plasmid and selection of the correct transgenic fly. All other genotypes were established through standard genetics. *repo-Gal4* was used to drive gene expression in the glial lineage. *UAS-eGFP* or *UAS-mRFP* were introduced to visualize and quantify tumour volume. *repo-Gal4;UAS-dEGFR$^{\lambda}$;UAS-Dp110^{CAAX}* (as previously described[24]) and *repo-Gal4;UAS-F3–T3* stocks were balanced over the *CyoWeeP* and *TM6B* balancers. *srl* RNAi lines were obtained from the Bloomington *Drosophila* Stock Center (BDSC) and the Vienna *Drosophila* Resource Center (VDRC): *P{KK100201}VIE-260B* (VDRC v103355), *y^1 sc* v^1; P{TRiP.GL01019}attP40* (BDSC 57043), *y^1 sc* v^1; P{TRiP.HMS00857}attP2* (BDSC 33914), and *y^1 sc* v^1; P{TRiP.HMS00858}attP2* (BDSC 33915). The following *ERR* RNAi lines were used: *y^1 v^1; P{TRiP.JF02431}attP2* (BDSC 27085), *y^1 v^1; P{TRiP.HMC03087}attP2* (BDSC 50686) and *P{KK108422}VIE-260B* (VDRC v108349). *y^1 v^1; P{UAS-GFP.VALIUM10}attP2* (BDSC 35786) was used as a control for RNAi experiments.

Fly culture, immunohistochemistry and imaging. Flies were mated and maintained at 29 °C. Fly larvae were retrieved at late third instar stage for brain dissections followed by fixation and immunohistochemical analysis. Larval brains were dissected, fixed and stained as previously described[61]. In brief, third instar larval brains were dissected in PBS, fixed in 4% paraformaldehyde solution for 20 min at room temperature, and incubated with primary antibodies, including: rat anti-phospho-histone H3 (Abcam, ab10543, 1:300) and mouse anti-Repo (Developmental Study Hybridoma Bank, 1:60) overnight at 4 °C and secondary antibody for 2 h at room temperature. Fluorescence images were acquired using a Leica SP8 confocal microscope.

Image analysis. To determine tumour volume, we acquired image stacks using a Leica SP8 confocal microscope with a *z*-step size of 5.0 µm per optical slice using a 20× objective throughout the entire thickness of the brain and ventral nerve cord. The confocal LIF files were converted into Imaris files using ImarisFileConverter 6.4.2. All subsequent image processing was conducted with Imaris 5.5 software. *z*-series stacks were used to make three-dimensional reconstructions. A smooth level of 1.0 was used on every measurement for consistency. Brain tumour volumes were quantified using three-dimensional reconstructions.

Statistical analysis. In general, two to four independent experiments were performed. Comparisons between groups were analysed by *t*-test with Welch correction (two-tailed, unequal variance) and/or the MWW non-parametric test when

appropriate. Results in graphs are expressed as mean ± s.d. or mean ± s.e.m. for the indicated number of observations. All statistical analyses were performed and *P* values were obtained using the GraphPad Prism software 6.0 or the R software (https://www.r-project.org) and are reported in Source Data.

Code availability. A collection of the R procedures to perform ee-MWW is available at http://github.com/miccec/yaGST. The *RGBM* package is available from CRAN at https://cran.r-project.org/web/packages/RGBM/index.html.

Data availability. Transcriptomic microarray gene expression data have been deposited in ArrayExpress with accession number E-MTAB-6037. Source data for western blot are provided in Supplementary Fig. 1. Source Data for Figs 1–4 and Extended Data Figs 1, 2, 4, 7–10 are included in the online version of the paper.

28. Isserlin, R., Merico, D., Voisin, V. & Bader, G. D. Enrichment Map — a Cytoscape app to visualize and explore OMICs pathway enrichment results. *F1000Res.* **3,** 141 (2014).
29. Smoot, M. E., Ono, K., Ruscheinski, J., Wang, P. L. & Ideker, T. Cytoscape 2.8: new features for data integration and network visualization. *Bioinformatics* **27,** 431–432 (2011).
30. Merico, D., Isserlin, R., Stueker, O., Emili, A. & Bader, G. D. Enrichment map: a network-based method for gene-set enrichment visualization and interpretation. *PLoS ONE* **5,** e13984 (2010).
31. Stransky, N., Cerami, E., Schalm, S., Kim, J. L. & Lengauer, C. The landscape of kinase fusions in cancer. *Nat. Commun.* **5,** 4846 (2014).
32. Yoshihara, K. *et al.* The landscape and therapeutic relevance of cancer-associated transcript fusions. *Oncogene* **34,** 4845–4854 (2015).
33. Iyer, M. K., Chinnaiyan, A. M. & Maher, C. A. ChimeraScan: a tool for identifying chimeric transcription in sequencing data. *Bioinformatics* **27,** 2903–2904 (2011).
34. Risso, D., Schwartz, K., Sherlock, G. & Dudoit, S. GC-content normalization for RNA-seq data. *BMC Bioinformatics* **12,** 480 (2011).
35. Ceccarelli, M. *et al.* Molecular profiling reveals biologically discrete subsets and pathways of progression in diffuse glioma. *Cell* **164,** 550–563 (2016).
36. Lum, P. Y. *et al.* Extracting insights from the shape of complex data using topology. *Sci. Rep.* **3,** 1236 (2013).
37. Roweis, S. T. & Saul, L. K. Nonlinear dimensionality reduction by locally linear embedding. *Science* **290,** 2323–2326 (2000).
38. Nielson, J. L. *et al.* Topological data analysis for discovery in preclinical spinal cord injury and traumatic brain injury. *Nat. Commun.* **6,** 8581 (2015).
39. Singh, G., Memoli, F. & Carlsson, G. E. Topological methods for the analysis of high dimensional data sets and 3D object recognition. In *SPBG* (eds Botsch, M. & Pajarola, R.) 91–100 (Citeseer, 2007).
40. Rizvi, A. H. *et al.* Single-cell topological RNA-seq analysis reveals insights into cellular differentiation and development. *Nat. Biotechnol.* **35,** 551–560 (2017).
41. Rolland, D. *et al.* Global phosphoproteomic profiling reveals distinct signatures in B-cell non-Hodgkin lymphomas. *Am. J. Pathol.* **184,** 1331–1342 (2014).
42. Kessner, D., Chambers, M., Burke, R., Agus, D. & Mallick, P. ProteoWizard: open source software for rapid proteomics tools development. *Bioinformatics* **24,** 2534–2536 (2008).
43. Fenyö, D. & Beavis, R. C. A method for assessing the statistical significance of mass spectrometry-based protein identifications using general scoring schemes. *Anal. Chem.* **75,** 768–774 (2003).
44. MacLean, B., Eng, J. K., Beavis, R. C. & McIntosh, M. General framework for developing and evaluating database scoring algorithms using the TANDEM search engine. *Bioinformatics* **22,** 2830–2832 (2006).
45. Keller, A., Nesvizhskii, A. I., Kolker, E. & Aebersold, R. Empirical statistical model to estimate the accuracy of peptide identifications made by MS/MS and database search. *Anal. Chem.* **74,** 5383–5392 (2002).
46. Nesvizhskii, A. I., Keller, A., Kolker, E. & Aebersold, R. A statistical model for identifying proteins by tandem mass spectrometry. *Anal. Chem.* **75,** 4646–4658 (2003).
47. Pedrioli, P. G. Trans-proteomic pipeline: a pipeline for proteomic analysis. *Methods Mol. Biol.* **604,** 213–238 (2010).
48. Fermin, D., Basrur, V., Yocum, A. K. & Nesvizhskii, A. I. Abacus: a computational tool for extracting and pre-processing spectral count data for label-free quantitative proteomic analysis. *Proteomics* **11,** 1340–1345 (2011).
49. Beausoleil, S. A., Villén, J., Gerber, S. A., Rush, J. & Gygi, S. P. A probability-based approach for high-throughput protein phosphorylation analysis and site localization. *Nat. Biotechnol.* **24,** 1285–1292 (2006).
50. Lee, S. B. *et al.* An ID2-dependent mechanism for VHL inactivation in cancer. *Nature* **529,** 172–177 (2016).
51. Sonoda, Y. *et al.* Formation of intracranial tumors by genetically modified human astrocytes defines four pathways critical in the development of human anaplastic astrocytoma. *Cancer Res.* **61,** 4956–4960 (2001).
52. Rutka, J. T. *et al.* Establishment and characterization of five cell lines derived from human malignant gliomas. *Acta Neuropathol.* **75,** 92–103 (1987).
53. Malina, A. *et al.* Adapting CRISPR/Cas9 for functional genomics screens. *Methods Enzymol.* **546,** 193–213 (2014).
54. Ran, F. A. *et al.* Genome engineering using the CRISPR–Cas9 system. *Nat. Protoc.* **8,** 2281–2308 (2013).
55. Zhao, X. *et al.* The HECT-domain ubiquitin ligase Huwe1 controls neural differentiation and proliferation by destabilizing the N-Myc oncoprotein. *Nat. Cell Biol.* **10,** 643–653 (2008).
56. Livak, K. J. & Schmittgen, T. D. Analysis of relative gene expression data using real-time quantitative PCR and the $2^{-\Delta\Delta C_T}$ method. *Methods* **25,** 402–408 (2001).
57. Ajaz, S., Czajka, A. & Malik, A. Accurate measurement of circulating mitochondrial DNA content from human blood samples using real-time quantitative PCR. *Methods Mol. Biol.* **1264,** 117–131 (2015).
58. Vazquez, F. *et al.* PGC1α expression defines a subset of human melanoma tumors with increased mitochondrial capacity and resistance to oxidative stress. *Cancer Cell* **23,** 287–301 (2013).
59. Subramanian, A. *et al.* Gene set enrichment analysis: a knowledge-based approach for interpreting genome-wide expression profiles. *Proc. Natl Acad. Sci. USA* **102,** 15545–15550 (2005).
60. Lasorella, A., Rothschild, G., Yokota, Y., Russell, R. G. & Iavarone, A. Id2 mediates tumor initiation, proliferation, and angiogenesis in Rb mutant mice. *Mol. Cell. Biol.* **25,** 3563–3574 (2005).
61. Zhu, S. *et al.* The bHLH repressor Deadpan regulates the self-renewal and specification of *Drosophila* larval neural stem cells independently of Notch. *PLoS ONE* **7,** e46724 (2012).

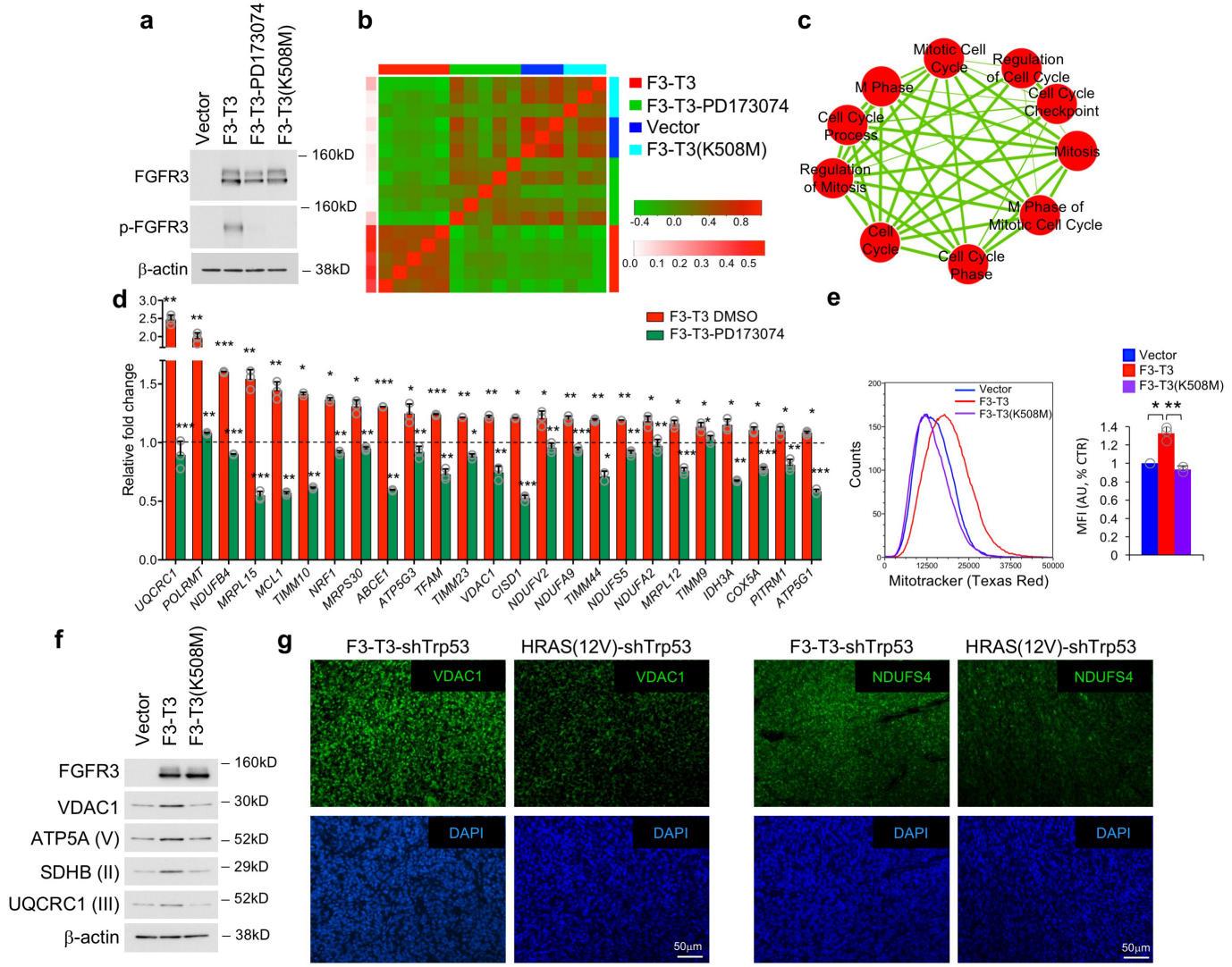

Extended Data Figure 1 | Activation of mitosis and mitochondria by F3–T3. a, Immunoblot analysis of FGFR3 and phospho-FGFR3 in F3–T3 human astrocytes treated with DMSO or PD173074, or human astrocytes expressing F3–T3(K508M) or vector. β-Actin is shown as a loading control. Experiment was repeated at least five times with similar results. **b**, Heat map of correlations among F3–T3 human astrocytes, F3–T3 human astrocytes treated with PD173074, and human astrocytes expressing vector or F3–T3(K508M). Top and right track colours represent sample type; left track colour scale represents correlation between each sample and the F3–T3 group. F3–T3 human astrocytes and F3–T3 human astrocytes treated with PD173074 ($n = 5$ biologically independent samples per group). Human astrocytes expressing vector or F3–T3(K508M) ($n = 3$ biologically independent samples per group). **c**, Enrichment map network of GO categories scoring as significant ($Q < 10^{-6}$ in each comparison) from three independent GSEAs (F3–T3 human astrocytes versus F3–T3 human astrocytes treated with PD173074; F3–T3- versus F3–T3(K508M)-expressing human astrocytes; F3–T3- versus vector-expressing human astrocytes). Nodes represent GO terms and lines indicate their connectivity. Size of nodes is proportional to enrichment significance and thickness of lines indicates the fraction of genes shared between the groups. **d**, RT–qPCR of vector- or F3–T3-expressing human astrocytes treated with vehicle (DMSO) or PD173074 for 12 h. Data are fold change relative to vector (dotted line) of one representative experiment out of two independent experiments (data are mean ± s.d., $n = 3$ technical replicates). P values were calculated using a two-tailed t-test with unequal variance; $^{*}P < 0.05$, $^{**}P < 0.01$, $^{***}P < 0.001$. For a complete list of P values see Source Data. **e**, Left, analysis of mitochondrial mass by MitoTracker FACS analysis in human astrocytes expressing F3–T3, F3–T3(K508M) or vector. Right, quantification of mean fluorescence intensity (MFI). Data are mean ± s.d. of three (vector and F3–T3) and two (F3–T3(K508M)) independent experiments. $^{*}P < 0.05$, $^{**}P < 0.01$; two-tailed t-test with unequal variance. **f**, Immunoblot analysis of mitochondrial proteins in human astrocytes expressing F3–T3, F3–T3(K508M) and vector. Experiment was repeated independently three times with similar results. **g**, Representative micrographs of VDAC1 and NDUFS4 immunofluorescence (top, green) in F3–T3;shTrp53 and HRAS(12V);shTrp53 mGSCs. DAPI staining of nuclei is shown as an indication of cellular density (bottom, blue). Experiment was repeated independently twice with similar results. Molecular weights are indicated on all immunoblots.

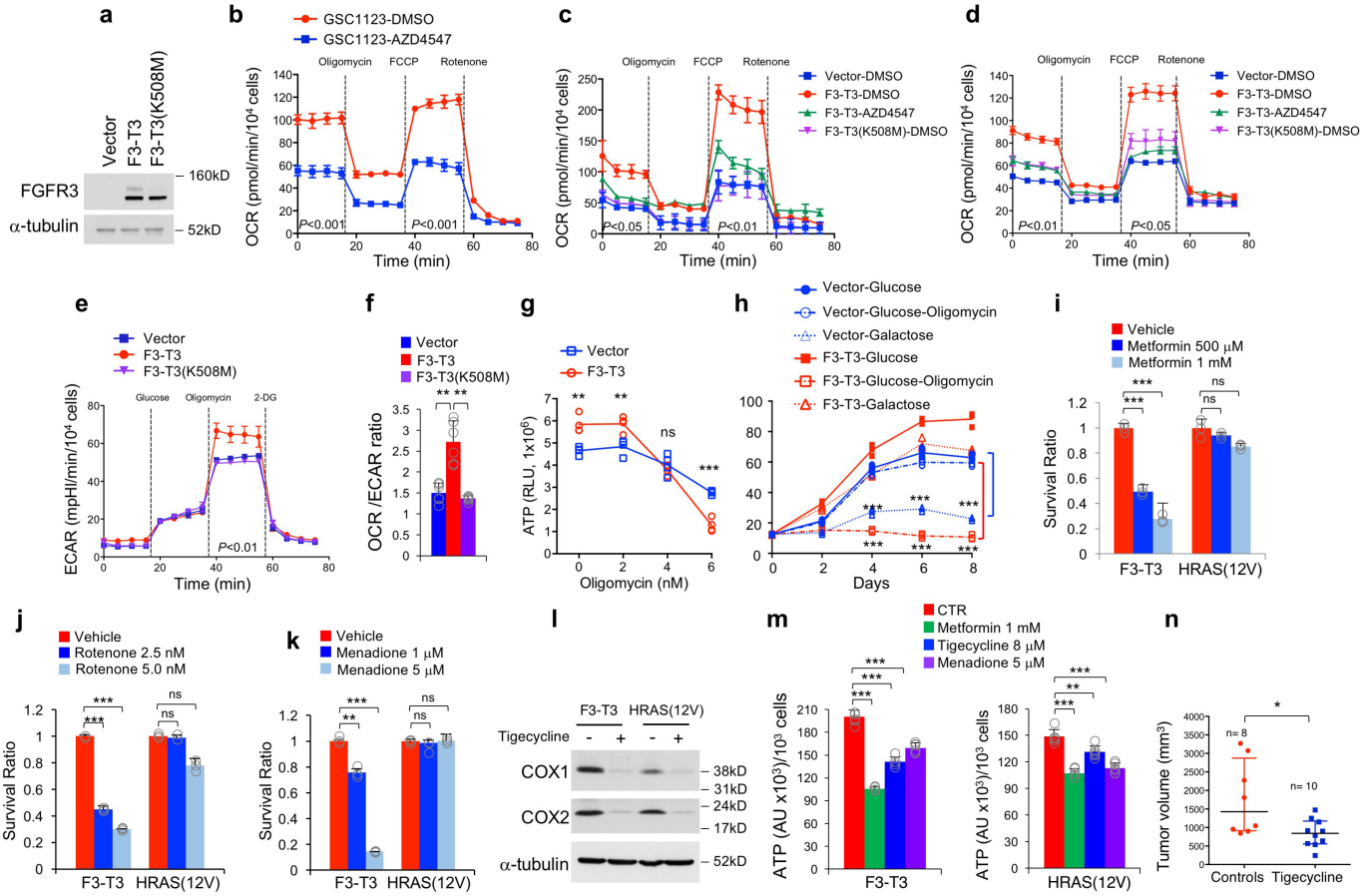

Extended Data Figure 2 | F3–T3 induces sensitivity to inhibitors of mitochondrial metabolism. a, Immunoblot analysis using the FGFR3 antibody in human astrocytes expressing vector, F3–T3 or F3–T3(K508M). α-Tubulin is shown as a loading control. Experiment was repeated five times with similar results. **b**, OCR of GSC1123 cells expressing F3–T3 in the presence or absence of AZD4547. Data are mean ± s.d. ($n = 6$ technical replicates) of one representative experiment out of two independent experiments. $P < 0.001$ for rate 1–4 and 9–12, two-tailed *t*-test with unequal variance. **c**, OCR of RPE cells expressing F3–T3, F3–T3(K508M) or the empty vector in the presence or absence of AZD4547. Data are mean ± s.d. ($n = 3$ technical replicates) of one representative experiment out of three independent experiments performed in triplicate with similar results. $P < 0.05$ for rate 1–4; $P < 0.001$ for rate 9–12; two-tailed *t*-test with unequal variance. **d**, OCR of U251 cells expressing F3–T3, F3–T3(K508M) or the empty vector in the presence or absence of AZD4547. Data are mean ± s.d. ($n = 3$ technical replicates) of one representative experiment out of two independent experiments performed in triplicate with similar results. $P < 0.01$ for rate 1–4; $P < 0.001$ for rate 9–12; two-tailed *t*-test with unequal variance. **e**, ECAR of human astrocytes expressing F3–T3, F3–T3(K508M) or the empty vector. Data are mean ± s.d. ($n = 3$ technical replicates) of one representative experiment out of two independent experiments performed in triplicate with similar results. $P < 0.01$ for rate 9–12; two-tailed *t*-test with unequal variance. **f**, Ratio between OCR (rate 4) and ECAR (rate 8) in human astrocytes expressing F3–T3, F3–T3(K508M) or vector. Data are mean ± s.d. ($n = 6$ replicates) of two independent experiments each performed in triplicate. $P < 0.01$; two-tailed *t*-test with unequal variance. **g**, Quantification of ATP production in human astrocytes expressing F3–T3 or vector following treatment with the indicated concentrations of oligomycin for 72 h. Data are independent technical replicates ($n = 4$) and means (connecting lines) of one representative experiment out of two independent experiments performed with similar results. $^{**}P < 0.01$; $^{***}P < 0.001$; two tailed *t*-test with unequal variance. **h**, Time-course analysis of cellular growth of human astrocytes expressing F3–T3 or vector cultured in the presence of glucose (25 mM) or galactose (25 mM) with or without oligomycin (100 nM). Data are independent technical replicates ($n = 3$) of one representative experiment out of two independent experiments performed with similar results. $^{***}P < 0.001$; two-tailed *t*-test with unequal variance. **i**–**k**, Survival ratio of F3–T3;shTrp53 and HRAS(12V);shTrp53 mGSCs treated for 72 h with vehicle or metformin (**i**), rotenone (**j**) or menadione (**k**) at the indicated concentrations. Data are mean ± s.d. ($n = 3$ technical replicates) of one representative experiment out of two independent experiments performed with similar results. $^{**}P < 0.01$; $^{***}P < 0.001$; two-tailed *t*-test with unequal variance. **l**, Western blot analysis of COX1 and COX2 proteins in F3–T3;shTrp53 and HRAS(12V);shTrp53 mGSCs treated with vehicle or tigecycline at a concentration of 8 μM for 72 h. α-Tubulin is shown as a loading control. Experiment was independently repeated twice with similar results. **m**, Quantification of cellular ATP in F3–T3;shTrp53 (left) and HRAS(12V);shTrp53 (right) mGSCs treated with vehicle or metformin (1 mM), tigecycline (8 μM) or menadione (5 μM) for 16 h. Data are mean ± s.d. of one experiment ($n = 6$ technical replicates). $^{**}P < 0.01$; $^{***}P < 0.001$; two-tailed *t*-test with unequal variance. **n**, Quantification of tumour volume of F3–T3;shTrp53 mGSCs in control and tigecycline-treated mice. Data are tumour volumes (median with interquartile range) at day 6 of treatment, a time when all mice were still in the study; $n = 8$ for control (median = 1,427 mm^3) and $n = 10$ for tigecycline-treated mice (median = 843.4 mm^3). $^{*}P < 0.05$; two-sided Mann–Whitney *U*-test. Molecular weights are indicated in immunoblots.

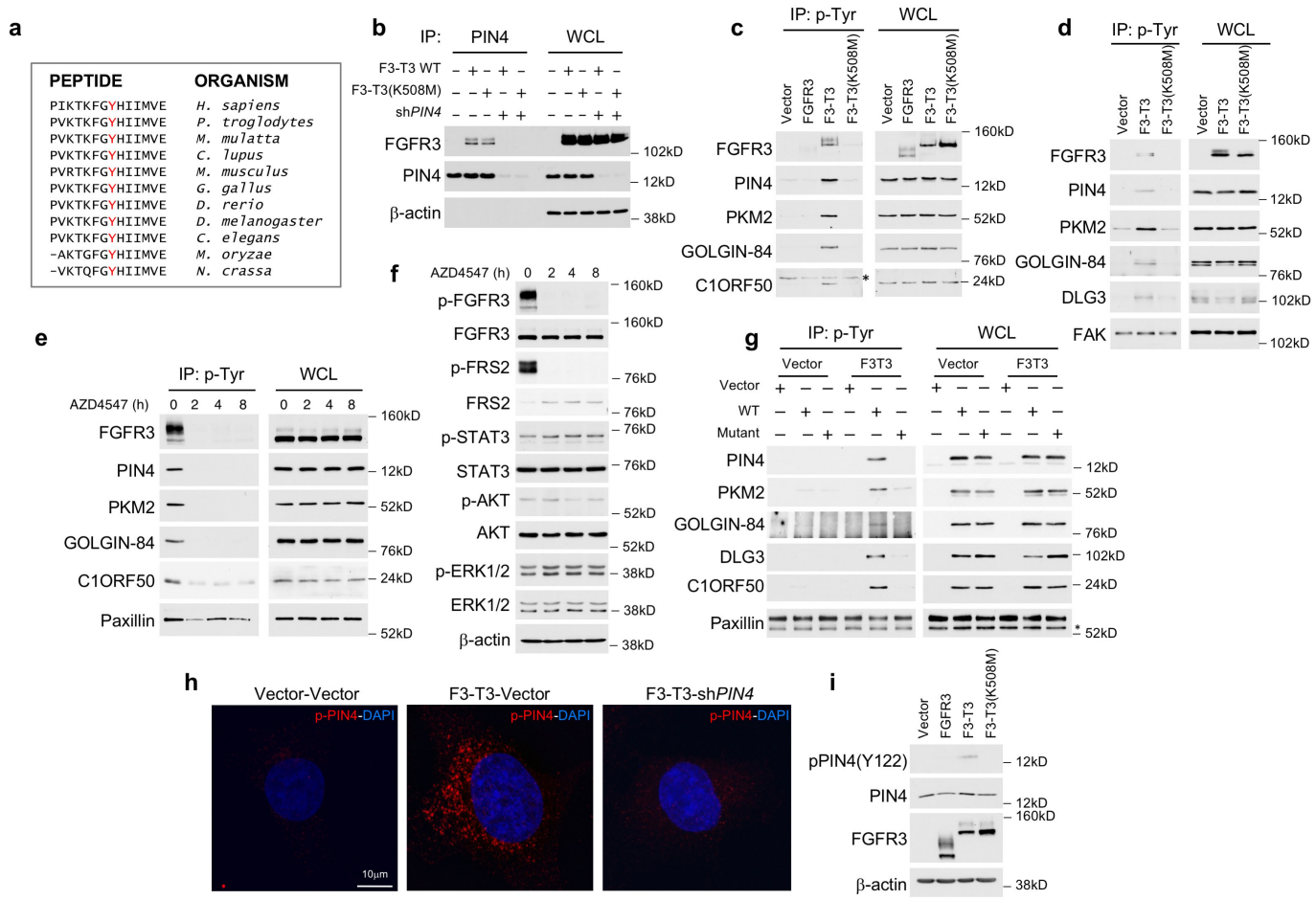

Extended Data Figure 3 | Phosphorylation of Y122 of PIN4 by F3–T3. **a**, Amino acid sequence flanking Y122 of PIN4 (in red) is evolutionarily conserved. **b**, Immunoprecipitation–western blot analysis of human astrocytes expressing F3–T3 or F3–T3(K508M) with or without silencing of endogenous *PIN4*. β-Actin is shown as a loading control. WCL, whole-cell lysate. **c**, Immunoblot analysis of phosphotyrosine immunoprecipitates (left) or whole-cell lysates (right from U87 glioma cells expressing empty vector, FGFR3, F3–T3 or F3–T3(K508M) using the indicated antibodies. The asterisk indicates a non-specific band. **d**, Immunoblot analysis of phosphotyrosine immunoprecipitates (left) or whole-cell lysates (right) from human astrocytes expressing empty vector, F3–T3 or F3–T3(K508M) using the indicated antibodies. FAK is shown as a loading control. **e**, Immunoblot analysis of phosphotyrosine immunoprecipitates (left) or whole-cell lysates (right) from GSC1123 cells expressing endogenous F3–T3 shows decreased phosphorylation of F3–T3 substrates following treatment with AZD4547 for the indicated times. Paxillin is shown as a loading control. **f**, Immunoblot analysis of canonical FGFR signalling proteins in GSC1123 cells treated with AZD4547 for the indicated time. β-Actin is shown as a loading control. **g**, Immunoblot analysis of phosphotyrosine immunoprecipitates from human astrocytes expressing F3–T3 or vector transduced with wild-type or the unphosphorylable Y to A F3–T3 kinase substrate mutants. Paxillin is shown as a loading control. The asterisk indicates a non-specific band. **h**, Confocal images of immunofluorescence staining using the phospho-PIN4(Y122)-specific antibody (red) in human astrocytes transduced with vector or F3–T3 without or with silencing of endogenous *PIN4*. Nuclei were stained with DAPI (blue). **i**, Immunoblot analysis of phospho-PIN4(Y122), total PIN4 and FGFR3 in SF126 cells transduced with FGFR3, F3–T3, F3–T3(K508M) or the empty vector. β-Actin is shown as a loading control. Molecular weights are indicated in all panels. Experiments in **b**–**g**, **i** were repeated independently three times with similar results. Experiment in **h** was repeated independently four times with similar results.

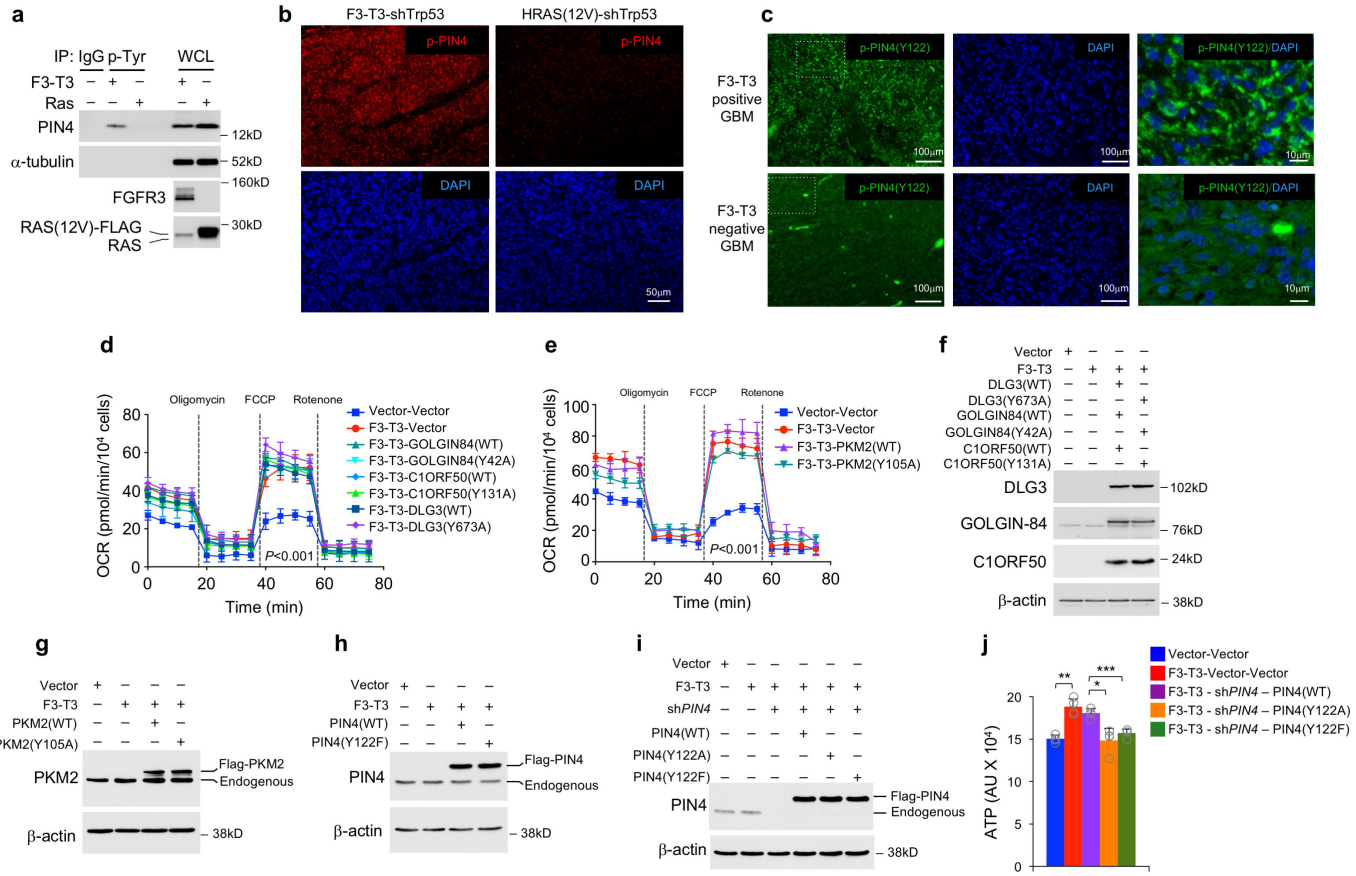

Extended Data Figure 4 | Functional analysis of tyrosine phosphorylation of F3–T3 kinase substrates. a, Western blot analysis of phosphotyrosine immunoprecipitation of F3–T3;shTrp53 and HRAS(12V);shTrp53 mGSCs using the PIN4 antibody. F3–T3 and HRAS(12V) expression are shown. α-Tubulin is shown as a loading control. **b**, Immunofluorescence images using the phospho-PIN4(Y122)-specific antibody (red, top) in tumours from F3–T3;shTrp53 and HRAS(12V)shTrp53 mGSCs. Nuclei were counterstained with DAPI (blue, bottom). Experiment was repeated independently twice with similar results. **c**, Left, representative images of phospho-PIN4(Y122) immunofluorescence in F3–T3-positive (top) and F3–T3-negative (bottom) GBM (green). Right, higher magnification images of phospho-PIN4(Y122)–DAPI co-staining depicting cytoplasmic localization of phospho-PIN4(Y122). Middle, DAPI staining of nuclei is shown as an indication of cellular density. **d**, Analysis of OCR in human astrocytes F3–T3 transduced with wild-type or the unphosphorylable Y to A mutant of GOLGIN84, C1orf50 and DLG3. Human astrocytes expressing the empty vector are included as a control. Data are mean ± s.d. ($n = 5$ technical replicates) of one representative experiment out of two independent experiments performed in triplicate with similar results. $P < 0.001$, rate 9–12 for vector versus each F3–T3 combination, two-tailed *t*-test with unequal variance. **e**, Analysis of OCR of human astrocytes expressing F3–T3 transduced with PKM2(WT), PKM2(Y105A) or the empty vector. Human astrocytes expressing the empty vector are included as control. Data are mean ± s.d. ($n = 3$ technical replicates) of one representative experiment out of three independent experiments; $P < 0.001$, rate 9–12 for vector versus each F3–T3 combination, two-tailed *t*-test with unequal variance. **f**, Immunoblot analysis of GOLGIN84, C1orf50 and DLG3 wild-type or Y to A mutants in human astrocytes experessing F3–T3 or vector. **g**, Immunoblot analysis of human astrocytes transduced with empty vector or F3–T3 expressing PKM2(WT) or PKM2(Y105A). **h**, Immunoblot analysis of human astrocytes transduced with F3–T3 or the empty vector for the expression of PIN4(WT) or PIN4(Y122F). **i**, Immunoblot analysis of PIN4 proteins in human astrocytes expressing F3–T3 following silencing of endogenous *PIN4* and reconstitution with PIN4(WT), PIN4(Y122A) or PIN4(Y122F). In **f**–**i**, β-actin is shown as a loading control. Molecular weights are indicated on all immunoblots. **j**, Quantification of ATP levels in human astrocytes treated as in **i**. Data are mean ± s.d. ($n = 4$ technical replicates) of one out of two independent experiments. $^*P < 0.05$; $^{**}P < 0.01$; $^{***}P < 0.001$; two-tailed *t*-test with unequal variance. Experiments in **a**, **f**–**i** were repeated independently three times with similar results.

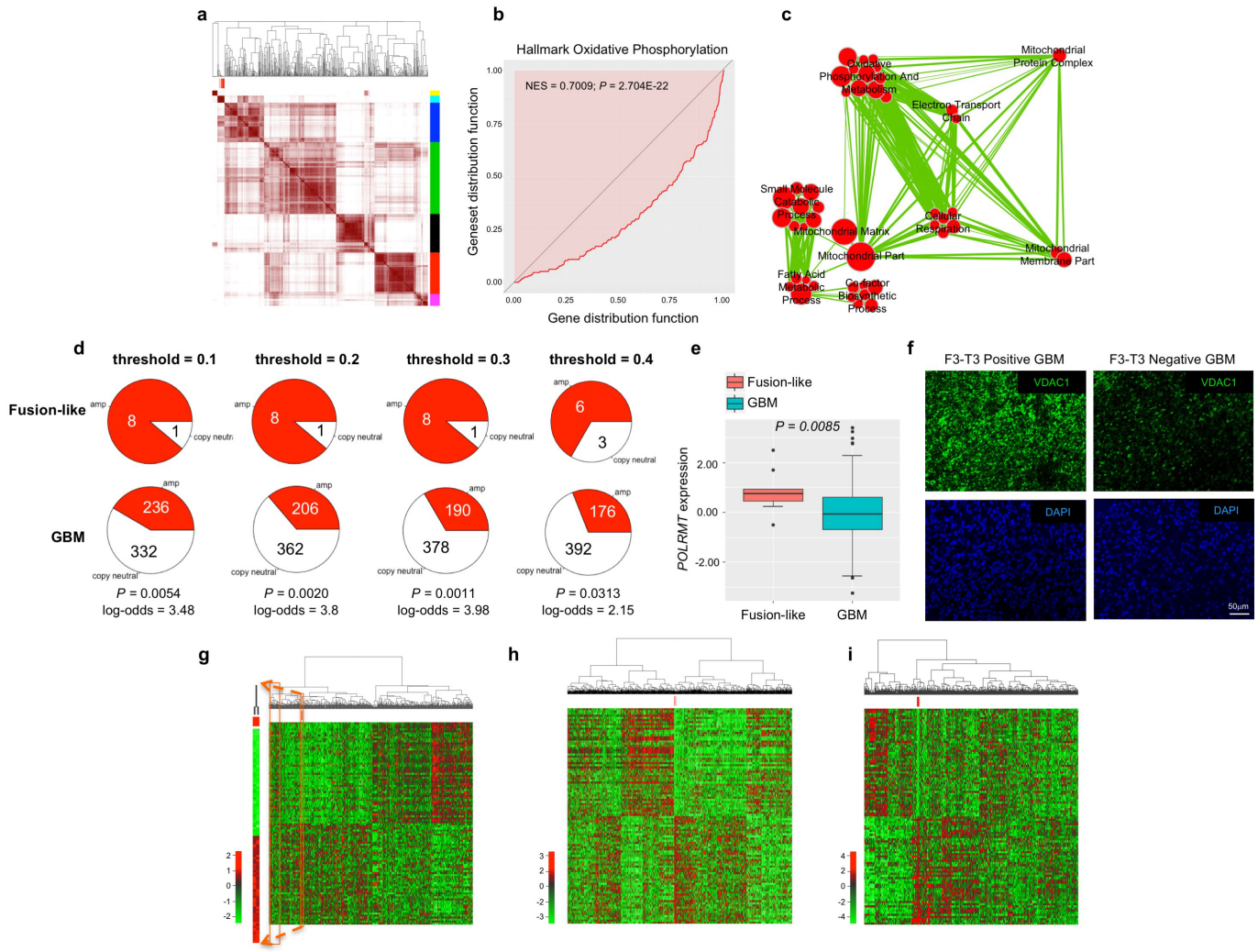

Extended Data Figure 5 | Transcriptomic analysis of F3–T3 fusion-positive and fusion-like GBM and validation of ee-MWW using different cancer-driving alterations. a, Consensus clustering on the Euclidean distance matrix based on the top and bottom 50 genes having the highest and lowest probability to be upregulated, respectively, in the nine F3–T3 fusion-positive GBM. The consensus matrix is obtained from 10,000 random samplings using 70% of the 544 samples. The nine F3–T3-positive GBM (in red) fall in one cluster (cyan). **b**, MWW enrichment plot of the 'hallmark oxidative phosphorylation' GO category in F3–T3-positive GBM. NES and *P*-values are indicated. **c**, Enrichment map network of statistically significant GO categories ($Q < 0.001$, NES > 0.6, upper-tailed MWW-GST) in nine fusion-like GBM. Nodes represent GO terms and lines demonstrate their connectivity. Size of nodes is proportional to number of genes in the GO category and thickness of lines indicates the fraction of genes shared between the groups. **d**, Analysis of copy number amplification of the *POLRMT* gene comparing fusion-like GBM with all other GBM at different thresholds for amplification detection on log-*R* ratio from single-nucleotide polymorphism arrays. *P* value and log-odds at different thresholds are indicated (Fisher's exact test). **e**, *POLRMT* gene expression in fusion-like GBM ($n = 9$) and the remaining samples ($n = 535$). Box plot spans the first to third quartiles and whiskers show the 1.5× interquartile range. *P* value, two-sided MWW test. **f**, Representative images of VDAC1 immunofluorescence in F3–T3-positive (green, left) and F3–T3-negative (right) GBM. DAPI staining of nuclei is shown as an indication of cellular density (blue, bottom). **g**, Hierarchical clustering of two GBM samples with a KRAS mutation (red) out of 544 samples. Heat map of the two KRAS mutant samples is enlarged to the left. **h**, Hierarchical clustering of five KRAS-mutated samples (red) in the invasive breast carcinoma (BRCA) cohort ($n = 1{,}093$). **i**, Hierarchical clustering of six EGFR–SEPT14-positive GBM samples (red) out of 544 samples. Data in **g**–**i**, were obtained using the Euclidean distance and Ward linkage method and are based on the top and bottom 50 genes having the highest and lowest probability to be upregulated, respectively.

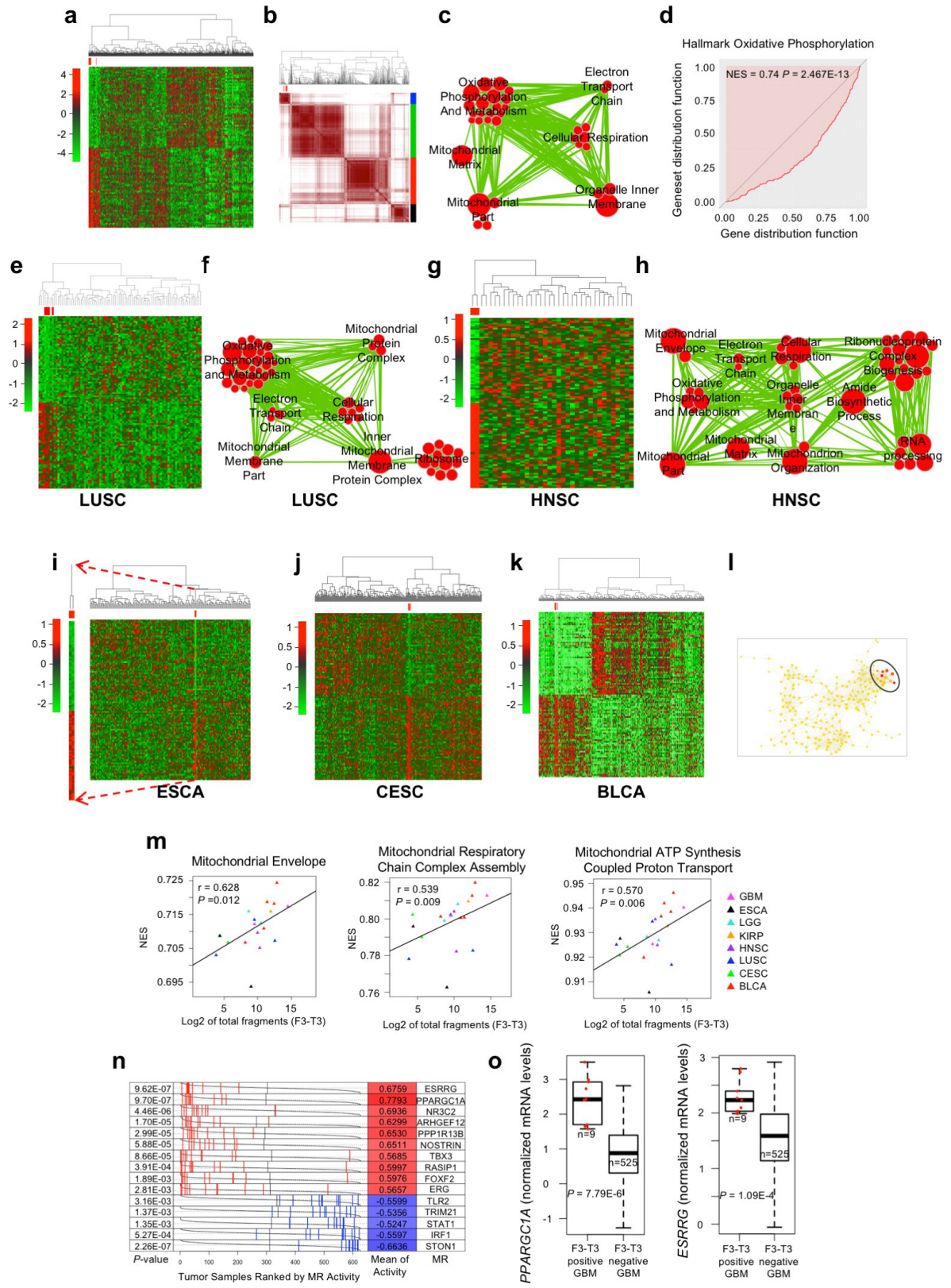

Extended Data Figure 6 | See next page for caption.

Extended Data Figure 6 | Pan-glioma and multi-cancer analysis of F3–T3 fusion-positive samples. a, **b**, Hierarchical (**a**) and consensus clustering (**b**) of 11 F3–T3-positive samples (red) out of 627 pan-glioma samples. The 11 F3–T3-positive samples (red) in **b** fall in one cluster (blue). **c**, Enrichment map network of statistically significant GO categories ($Q < 0.001$, NES > 0.6; upper-tailed MWW-GST) in the 11 F3–T3 fusion-positive pan-glioma samples. Nodes represent GO terms and lines demonstrate their connectivity. Size of nodes is proportional to number of genes in the GO category and thickness of lines indicates the fraction of genes shared between the groups. **d**, MWW enrichment plot of the 'hallmark oxidative phosphorylation' GO category in F3–T3-positive samples in the pan-glioma cohort. **e**, Hierarchical clustering of four F3–T3-positive (red) samples out of 86 lung squamous cell carcinoma (LUSC) samples. **f**, Enrichment map network of statistically significant GO categories ($Q < 0.001$, NES > 0.6; upper-tailed MWW-GST) in four F3–T3-positive LUSC Nodes represent GO terms and lines demonstrate their connectivity. Size of nodes is proportional to number of genes in the GO category and thickness of lines indicates the fraction of genes shared between the groups. **g**, Hierarchical clustering of two F3–T3-positive, human papilloma virus (HPV)-positive head and neck squamous cell carcinoma (HNSC) samples (in red) out of 36 samples. **h**, Enrichment map network of statistically significant GO categories ($Q < 0.001$, NES > 0.6; upper-tailed MWW-GST) in two F3–T3-positive HNSC samples. Nodes represent GO terms and lines demonstrate their connectivity. Size of nodes is proportional to number of genes in the GO category and thickness of lines indicates the fraction of genes shared between the groups. **i**, Hierarchical clustering of two F3–T3-positive samples (red) out of 184 oesophageal carcinoma (ESCA) samples. Heat maps of the two F3–T3-positive samples are enlarged to the left. **j**, Hierarchical clustering of four F3–T3-positive samples (red) out of 305 cervical squamous cell carcinoma and endocervical adenocarcinoma (CESC) samples. **k**, Hierarchical clustering of five F3–T3-positive samples (red) out of 408 urothelial bladder carcinoma (BLCA) samples. **l**, TDA network of pan-glioma samples ($n = 627$) reconstructed using variance normalized Euclidean distance and locally linear embedding as filter function. The nodes containing F3–T3-positive samples are highlighted in red. **m**, Correlation between the expression of F3–T3 ($\log_2$ of total fragment, x axis) and NES (y axis) of three top ranking mitochondrial functional categories in a multi-cancer cohort including F3–T3-positive samples ($n = 19$) from eight tumour types (r and P values are indicated, upper-tailed Spearman's rank correlation test). **n**, Analysis of the activity of master regulators in the pan-glioma cohort ($n = 627$ glioma). Grey curves represent the activity of each master regulator with tumour samples ranked according to master regulator activity. Red and blue lines indicate individual F3-T3-positive GBM samples displaying high and low master regulator activity, respectively. P values, two-sided MWW test, for differential activity (left) and mean of the activity (right) of the master regulator in F3–T3-positive versus F3–T3-negative samples are indicated. **o**, Gene expression analysis of *PPARGC1A* and *ESRRG* genes in F3–T3-positive and F3–T3-negative GBM; $n = 9$ F3–T3-positive tumours; $n = 525$ F3–T3-negative tumours. Box plot spans the first to third quartiles and whiskers show the 1.5× interquartile range. P value, two-sided MWW test. Data in **a**, **e**, **g**, **i**–**k**, were obtained using the Euclidean distance and Ward linkage method and are based on the top and bottom 50 genes having the highest and lowest probability to be upregulated, respectively.

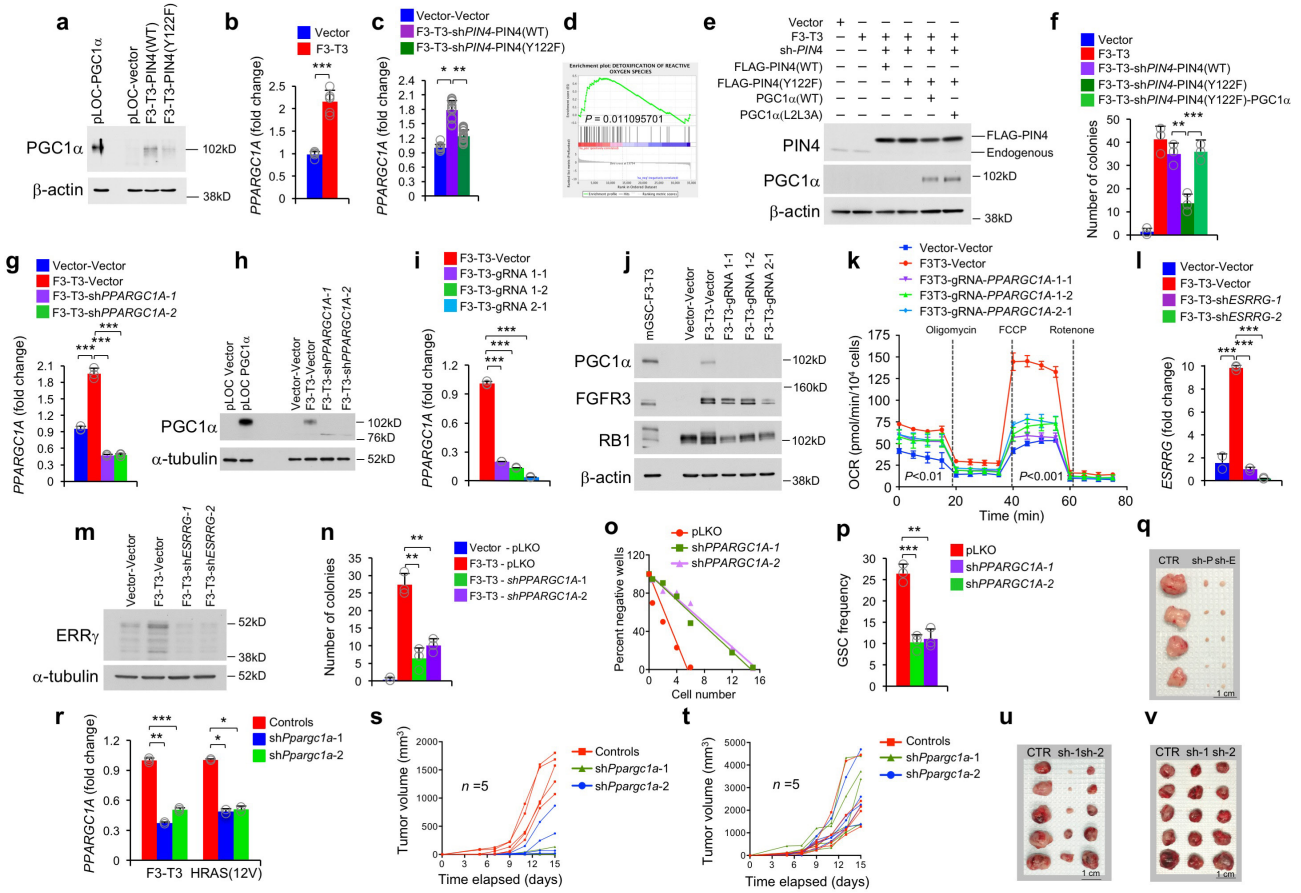

Extended Data Figure 7 | PGC1α and ERRγ are required for mitochondrial metabolism and tumorigenesis of cells transformed by F3–T3. a, Immunoblot of endogenous PGC1α in human astrocytes expressing F3–T3 following silencing of *PIN4* and reconstitution with wild-type or PIN4(Y122F). Exogenous expression of PGC1α in human astrocytes is included as positive control. Experiment was independently repeated three times with similar results. **b**, RT–qPCR of *PPARGC1A* in human astrocytes expressing F3–T3 or vector. Data are mean ± s.d. ($n = 6$ replicates) from two independent experiments each performed in triplicate. **c**, RT–qPCR of *PPARGC1A* in human astrocytes expressing F3–T3 treated as in **a**. Data are mean ± s.d. ($n = 4$ biological replicates) from four independent experiments. **d**, GSEA shows upregulation of ROS detoxification genes in human astrocytes expressing F3–T3 ($n = 5$ biological replicates) compared with vector ($n = 3$ biological replicates). Nominal *P* value is indicated. **e**, Immunoblot of Flag-PIN4 (wild-type and Y122F) and PGC1α (wild-type and L2L3A) in human astrocytes expressing F3–T3 after silencing of *PIN4*. Experiment was repeated twice independently with similar results. **f**, Soft agar colony-forming assay of human astrocytesF3–T3 following silencing of *PIN4* and reconstitution with wild-type or Y122F Flag-PIN4 in the presence or the absence of PGC1α. Data are mean ± s.d. ($n = 3$ technical replicates) from one representative experiment out of two independent experiments. **g**, RT–qPCR of *PPARGC1A* in human astrocytes expressing vector or F3–T3 transduced with *PPARGC1A* shRNA1 or *PPARGC1A* shRNA2 lentivirus. Data are mean ± s.d. ($n = 3$ technical replicates) from one representative experiment. **h**, Immunoblot analysis of PGC1α in HA-F3–T3 treated as in **g**. Experiment was repeated two times independently with similar results. Exogenous expression of PGC1α is included as positive control. Experiment was repeated twice independently with similar results. **i**, RT–qPCR of *PPARGC1A* in F3–T3 human astrocytes expressing two independent gRNAs against *PPARGC1A* (*PPARGC1A* gRNA1, two clones; *PPARGC1A* gRNA2, 1 clone) or the empty vector. Data are mean ± s.d. ($n = 3$ technical replicates) from one representative experiment. **j**, Western blot of cells treated as in (**i**) using the indicated antibodies. Experiment was repeated twice independently with similar results. **k**, OCR of human astrocytes expressing vector or F3–T3 transduced with *PPARGC1A* gRNA1 or gRNA2. Data are mean ± s.d. ($n = 5$ technical replicates) from one representative experiment out of two independent experiments. $P < 0.001$ for rate 1–4 and 9–12; two-tailed *t*-test with unequal variance. **l**, RT–qPCR of *ESRRG* in human astrocytes expressing vector or F3–T3 infected with *ESRRG* shRNA1 or *ESRRG* shRNA2 lentiviruses. Data are mean ± s.d. ($n = 3$ technical replicates) from one representative experiment. **m**, Immunoblot analysis of ERRγ in human astrocytes expressing F3–T3 treated as in **l**. Experiment was repeated twice independently with similar results. **n**, Soft agar colony-forming assay of human astrocytes treated as in Fig. 3g. Data are mean ± s.d. ($n = 3$ technical replicates) of one representative experiment out of two independent experiments performed in triplicate. **o**, GSC1123 cells were transduced with *PPARGC1A* shRNA lentiviruses or the empty vector. Cells were analysed by *in vitro* LDA. Representative regression plot used to calculate the frequency of gliomaspheres in 96-well cultures from three independent infections. **p**, Bar graph shows the frequency of gliomaspheres from three independent infections analysed by LDA as shown in **o**. Data are mean ± s.d. ($n = 3$ biological replicates). **q**, The photograph shows tumours generated by human astrocytes F3–T3 transduced with *PPARGC1A* shRNA1, *ESRRG* shRNA1 or vector lentivirus in Fig. 3i at the time of mouse euthanasia. sh-P, *PPARGC1A* shRNA1; sh-E, *ESRRG* shRNA1. **r**, RT–qPCR of *Ppargc1a* in F3–T3-shTrp53 and HRAS(12V) shTrp53 mGSCs transduced with *Ppargc1a* shRNA1 or *Ppargc1a* shRNA2 lentivirus. Data are mean ± s.d. ($n = 3$ technical replicates) of one representative experiment. **s**, Tumour volume of F3–T3-shTrp53 mGSCs expressing a pLKO-vector ($n = 5$), *Ppargc1a* shRNA1 ($n = 5$) or *Ppargc1a* shRNA2 ($n = 5$). Data are the tumour growth curve of individual mice. **t**, Tumour volume of mice injected subcutaneously with HRAS(12V);shTrp53 mGSCs expressing pLKO-vector ($n = 5$) or *Ppargc1a* shRNA1 ($n = 5$) or *Ppargc1a* shRNA2 ($n = 5$). Data are tumour growth curve of individual mice; NS, not significant, two-tailed *t*-test with unequal variance (time points 1–7). **u**, Photograph shows tumours generated from F3–T3;shTrp53 mGSCs transduced with *Ppargc1a* shRNA1 or *Ppargc1a* shRNA2 or vector lentivirus in **s** at the time of mouse euthanasia. **v**, Photograph shows tumours generated by HRAS(12V) shTrp53 mGSCs transduced with *Ppargc1a* shRNA1 or *Ppargc1a* shRNA2 or vector lentivirus in **t** at the time of mouse euthanasia. Molecular weights are indicated and β-actin or α-tubulin is shown as a loading control in all immunoblots. $^*P < 0.05$, $^{**}P < 0.01$, $^{***}P < 0.001$; two-tailed *t*-test with unequal variance.

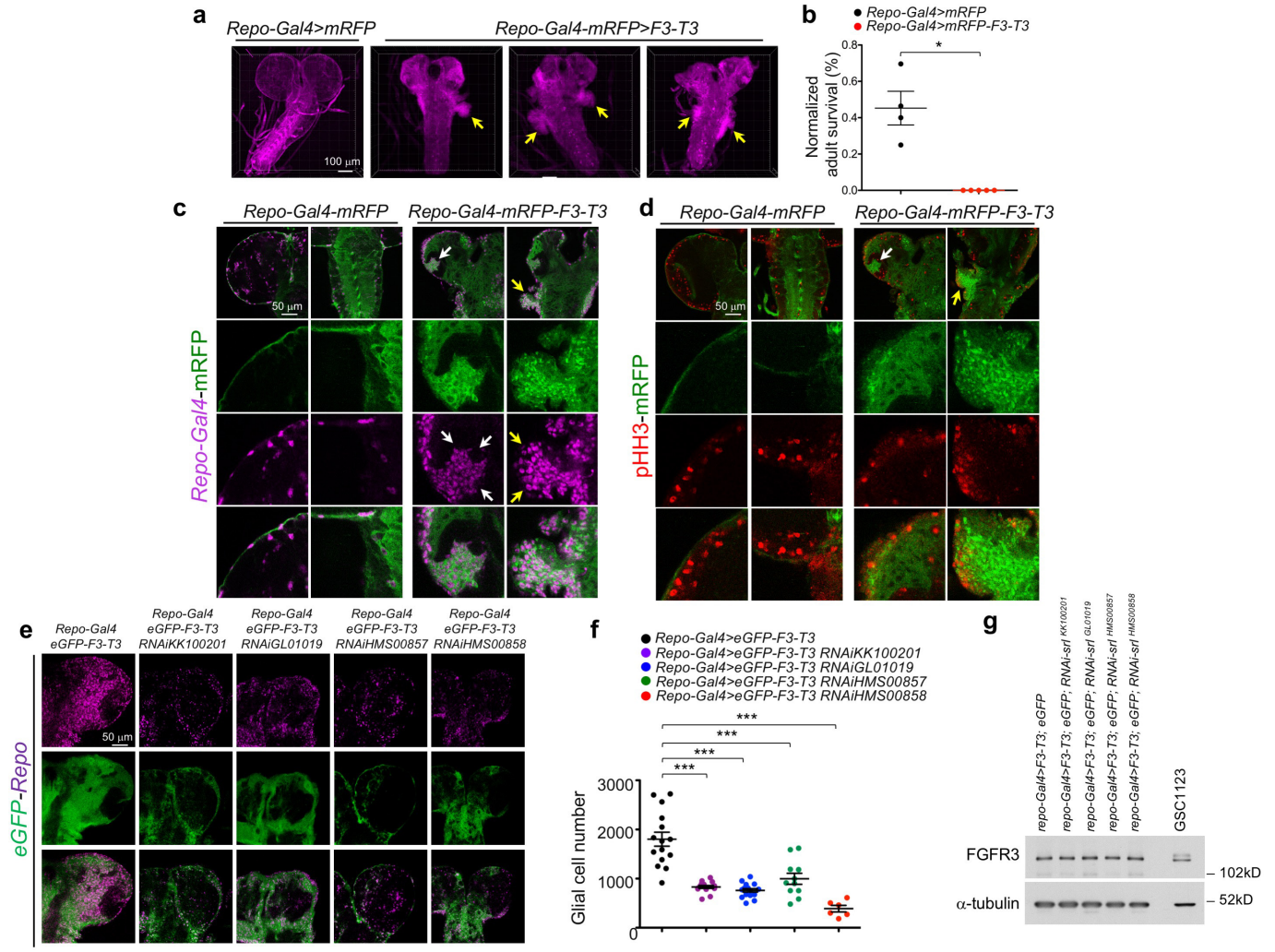

Extended Data Figure 8 | *Drosophila* PGC1α-homologue *spargel* (*srl*) mediates F3–T3-induced tumour growth. a, Optical projections of whole brain–ventral nerve cord complexes from *Drosophila* larvae. Expression of the F3–T3 fusion oncogene using the *repo-Gal4* (*repo-Gal4*>F3–T3) pan-glial driver induced pathological changes in brain and ventral nerve cord with ectopic tissue protrusions (yellow arrows) due to excessive glial cell proliferation and accumulation. **b**, Survival of larvae bearing F3–T3-driven glial tumours. Larvae bearing F3–T3-driven glial tumours die before developing into adulthood (biologically independent samples: $n = 87$, *Repo-Gal4* > mRFP; $n = 77$, *Repo-Gal4* > mRFP-F3-T3). Data are shown as mean ± s.e.m. $^*P < 0.05$; two-tailed *t*-test with unequal variance. Individual dots represent the fraction of surviving animals. **c**, Glial expression of F3–T3 resulted in increased total glial cell number ($Repo^+mRFP^+$ cells) compared to controls. Note the excessive accumulation of glial cells in the brain lobe (white arrows) and ventral nerve cord (yellow arrows). **d**, Glial expression of F3–T3 increases glial cell proliferation ($mRFP^+$ phosphorylated histone $H3^+$ (phospho-$HH3^+$) cells) compared to control. Note the excessive accumulation of glial cells in the brain lobe (white arrows) and ventral nerve cord (yellow arrows). **e**, Glia-specific *srl* knockdown in F3–T3-induced glial tumours resulted in decreased total glial number ($Repo^+eGFP^+$ cells) compared to controls. **f**, Quantification of glia number in control and *srl*-deficient tumours. $n = 15$ for *repo-Gal4*>F3–T3; $n = 15$ for *repo-Gal4*>F3–T3 *RNAi-KK100201*; $n = 16$ for *repo-Gal4*>F3–T3;*RNAi-GL01019*; $n = 11$, for *repo-Gal4*>F3–T3;*RNAi-HMS00857*; $n = 6$ for *repo-Gal4*>F3–T3;*RNAi-HMS00858*. Data are shown as mean ± s.e.m. $^{***}P < 0.001$; two-tailed *t*-test with unequal variance. **g**, Western blot analysis of the F3–T3 protein in *repo-Gal4>F3–T3* and *repo-Gal4>F3–T3;RNAi-srl Drosophila* brains. The expression of F3–T3 in human GSC1123 cells is shown as a positive control for F3–T3 and α-tubulin is shown as a loading control. Experiments in **c**–**e**, **g** were performed twice.

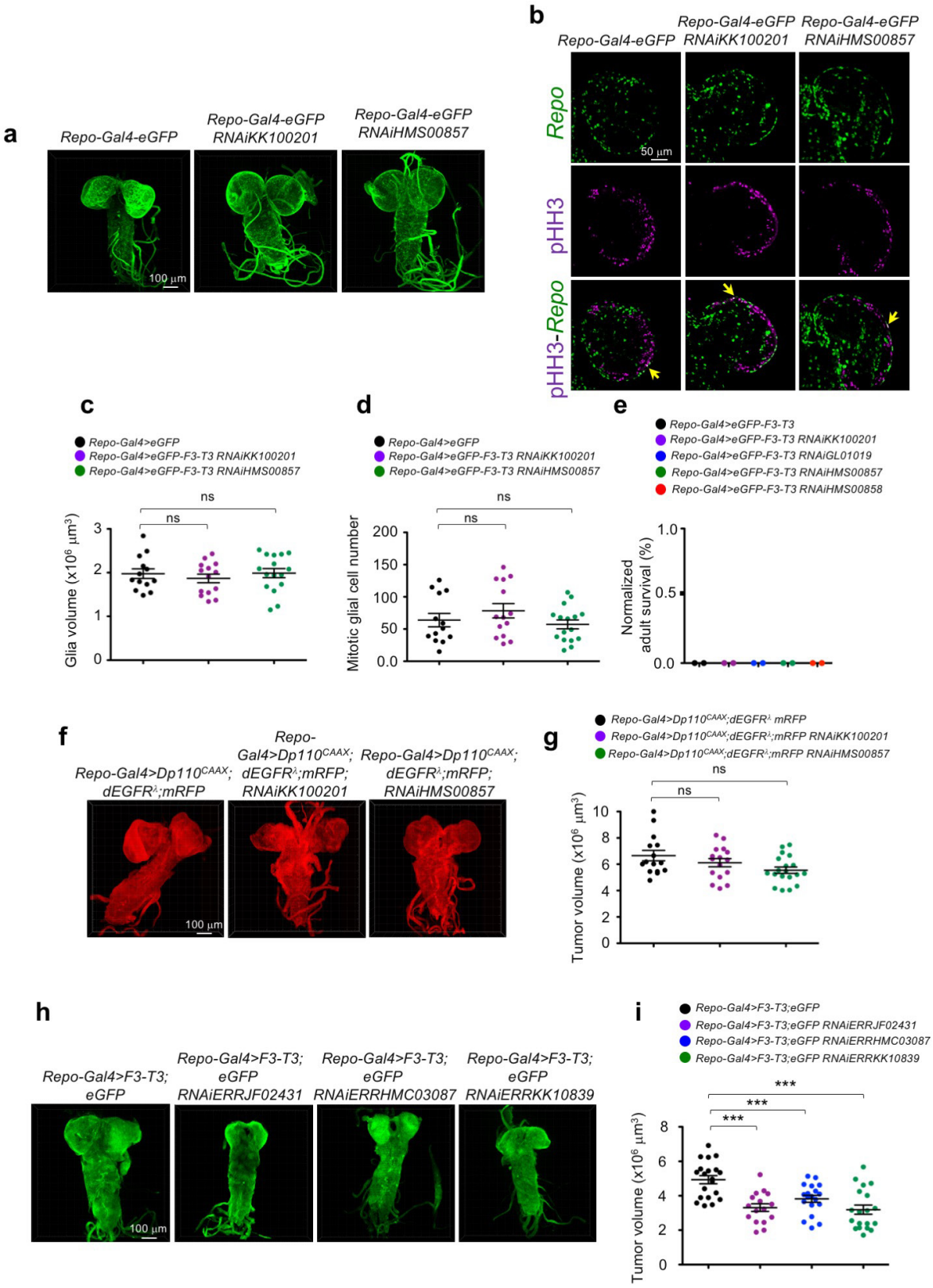

Extended Data Figure 9 | See next page for caption.

Extended Data Figure 9 | Glia-specific knockdown of *srl* has little to no effect on EGFR–PI3K-induced tumour growth but glia-specific knockdown of *ERR* inhibits F3–T3-induced tumour growth. a, Optical projections of whole brain–ventral nerve cord complexes from larvae with control and *srl*-deficient glia. **b**, Glia-specific *srl* knockdown in larval brains did not significantly affect the overall glial population ($Repo^+$ cells) nor the mitotic index of glial cells ($Repo^+$ phospho-$HH3^+$ cells, yellow arrows). **c**, Quantification of glia volume in larval brains with control and *srl*-deficient glia; $n = 13$ for *repo-Gal4>eGFP*; $n = 14$ for *repo-Gal4>eGFP;RNAi-KK100201;* and $n = 16$, for *repo-Gal4>eGFP;RNAi-HMS00857*. Data are mean ± s.e.m. NS, not significant; two-tailed *t*-test with unequal variance. **d**, Quantification of proliferating glia number ($Repo^+$; phospho-$HH3^+$ cells) in larval brains with control and *srl*-deficient glia; $n = 13$ for *repo-Gal4>eGFP*; $n = 14$ for *repo-Gal4> eGFP;RNAi-KK100201*; and $n = 16$ for *repo-Gal4> eGFP;RNAi-HMS00857*. Data are mean ± s.e.m. NS, not significant; two-tailed *t*-test with unequal variance. **e**, Adult lethality in repo-Gal4>F3–T3 and repo-Gal4>F3–T3;RNAi-*srl* larvae ($n > 100$). **f**, Optical projections of control and *srl*-deficient brain tumours from *repo-Gal4>*$Dp110^{CAAX}$*;*$dEGFR^{\lambda}$*;mRFP* larvae. **g**, Quantification of tumour volume in control and *srl*-deficient tumours; $n = 15$ for *repo-Gal4>*$Dp110^{CAAX}$*;*$dEGFR^{\lambda}$*;mRFP*; $n = 16$ for *repo-Gal4>*$Dp110^{CAAX}$*;*$dEGFR^{\lambda}$*;mRFP;RNAi-KK100201*; $n = 19$ for *repo-Gal4>-*$Dp110^{CAAX}$*;*$dEGFR^{\lambda}$*;mRFP;RNAi-HMS00857*. Data are mean ± s.e.m. NS, not significant; two-tailed *t*-test with unequal variance. **h**, Optical projections of brain tumours from *Drosophila* larvae *repo-Gal4*>F3–T3 and *repo-Gal4*>F3–T3;*RNAi-ERR*. RNAi-mediated knockdown of *ERR* reduces the volume of F3–T3-induced glial tumours. **i**, Quantification of tumour volume in the control and *ERR*-deficient tumours; $n = 20$ for *repo-Gal4*>F3–T3; $n = 16$ for *repo-Gal4*>F3–T3*;RNAi-JF02431*; $n = 19$, for *repo-Gal4*>F3–T3*;RNAi-HMC03087*; $n = 19$, for *repo-Gal4*>F3–T3*;RNAi-KK10839*). $***P < 0.001$; two-tailed *t*-test with unequal variance. In all experiments *n* are biologically independent animals. Experiments in **a**, **b**, **f**, **h**, were repeated twice with similar results.

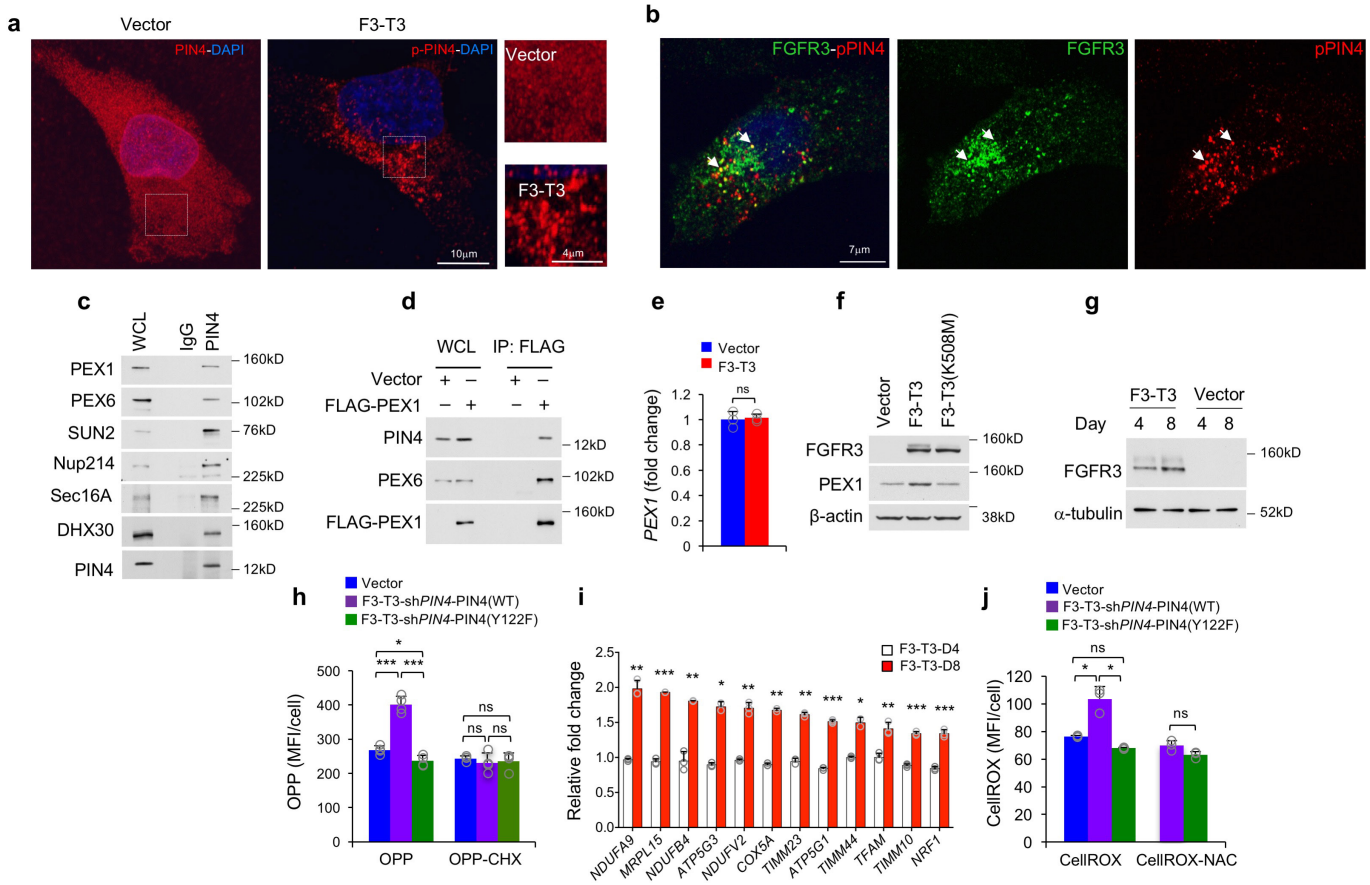

Extended Data Figure 10 | Acute expression of F3–T3 fusion induces peroxisome biogenesis through phosphorylation of PIN4(Y122). a, Representative confocal images (maximum intensity) of immunofluorescence staining for total PIN4 (PIN4, red, left) and phospho-PIN4(Y122) (p-PIN4, red, middle panel) in human astrocytes expressing the empty vector and F3–T3. Right, higher magnification of dotted boxes. Nuclei were counterstained with DAPI (blue). Experiment was repeated independently twice with similar results. **b**, Maximum intensity of confocal images of double immunofluorescence staining for FGFR3 (green, middle) and phospho-PIN4(Y122) (red, right) in human astrocytes expressing F3–T3. Arrows indicate protein co-localization. Experiment was repeated independently twice with similar results. **c**, Co-immunoprecipitation from H1299 cells using the PIN4 antibody. Endogenous PIN4 immunocomplexes and input (WCL) were analysed by western blot using the indicated antibodies. Input is 10% for PEX1, PEX6, SUN2 and NUP214; 5% for SEC16A and DHX30; 2% for PIN4. **d**, Western blot analysis of co-immunoprecipitation of exogenous Flag-PEX1 in human astrocytes expressing F3–T3. WCL: 1% for PIN4 and 10% for PEX1 and PEX6. Experiment was repeated independently four times with similar results. **e**, RT–qPCR of *PEX1* in human astrocytes expressing F3–T3 or vector. Data are mean ± s.d. ($n = 3$ technical replicates) of one representative experiment out of three independent experiments performed in triplicate. **f**, Western blot analysis of PEX1 expression in human astrocytes transduced with F3–T3, F3–T3(K508M) or the empty vector. β-Actin is shown as a loading control. Experiment was repeated independently three times with similar results. **g**, Time-course analysis of F3–T3 expression in human astrocytes by western blot. α-Tubulin is shown as a loading control. Experiment was repeated independently twice with similar results. **h**, Quantification of protein biosynthesis by OPP incorporation measured by high-content fluorescent microscopy in human astrocytes reconstituted with PIN4(WT) or PIN4(Y122F) after silencing of the endogenous *PIN4* and acutely transduced with F3–T3 or vector. Representative bar plots ($n = 4$ technical replicates) from one out of three independent experiments. $^{*}P < 0.05$, $^{***}P < 0.001$; two-tailed *t*-test with unequal variance. CHX-treated cultures were used as negative controls. **i**, Time-course expression analysis by RT–qPCR of the indicated mitochondrial genes in human astrocytes expressing F3–T3 or empty vector. Data are mean ± s.d. ($n = 3$ technical replicates) of one representative experiment out of two independent experiments performed in triplicate. Values were normalized to vector (dotted line). $^{*}P < 0.05$, $^{**}P < 0.01$, $^{***}P < 0.001$; two-tailed *t*-test with unequal variance. **j**, Quantification of cellular ROS (measured by high-content microscopy) in human astrocytes reconstituted with PIN4(WT) or PIN4(Y122F) after silencing of the endogenous *PIN4* and acutely transduced with F3–T3 or vector. Representative bar plots from one out of three independent experiments. Data are mean ± s.d. ($n = 3$ technical replicates). $^{*}P < 0.05$; two-tailed *t*-test with unequal variance. *N*-acetyl-L-cysteine-treated cultures were used as negative controls. Molecular weights are indicated in all immunoblots.